Implementing the State Space Approach for Controlling a Suspension System in KAGRA
(KAGRAにおける防振装置制御に対する状態空間モデルの適用)

Author: Ryohei Kozu
Supervisor: Takaaki Kajita

Department of Physics
School of Science
The University of Tokyo

January 4th, 2019

Abstract

In 1915, A. Einstein published General Relativity as a theory of the relationship between spacetime and matter [1,2]. He predicted the existence of gravitational waves as one of the consequences of general relativity. In 2015, LIGO (Laser Interferometer Gravitational-Wave Observatory) directly detected the gravitational wave event from a binary black hole (BH) merger for the first time [3]. This event not only served as a verification of Einstein's general relativity theory but also turned to be a major discovery of the first direct observation of BHs. It is the beginning of gravitational wave astronomy.

My research focuses on two independent topics. One is on installation work for a gravitational wave detector and the other is on mathematical model of a suspension which is a critical piece for gravitational wave detectors.

In Japan, a gravitational wave detector called KAGRA is currently under construction. KAGRA is different from other gravitational wave detectors in that it is in the basement and it uses cryogenic mirrors. All mirrors in KAGRA are suspended to isolate vibration and they designed mainly three kinds of suspensions; Type A, Type B and Type Bp. I installed Type B suspensions which hang the Beam Splitter (BS) and the Signal Recycling Mirrors (SRs) in cooperation with the NAOJ staff.

Measuring the actual transfer function is a good way to know the feature of the suspension in frequency space. However, when we start an observing run, we cannot use the real suspension in KAGRA. So it is significant to build a model in state space. In state space, one can use ABCD matrices which includes the information of suspensions. And from this, one can simulate the transfer function and frequency response without using real one. To know the time series of suspension, A. Shoda, Y. Fuji and I implemented the state space to control the suspension. To build the model, we used Matlab and Mathematica.

To check the behavior of time series, I checked the Yaw motion of SR3 intermediate mass (IM) because the Yaw has less coupling and it was expected to act better than other degree of freedoms. The SR3 IM Yaw time series of the step response matched for the first 20 seconds.

Contents

1 Detection of Gravitational Waves

1.1 Gravitational Waves

Gravitational waves, which propagate at the speed of light, are distortions of spacetime, which were predicted by Albert Einstein using his theory of General Relativity in 1916.

In 1687, I. Newton published "Philosophiæ Naturalis Principia Mathematica" and this was the origin of what is known as "Classical Mechanics". In this theory, space, time and matter are independent of each other. The relationship between the gravitational potential ϕ and matter was described as

$$\Delta\phi = 4\pi G\rho,$$

where G is the Newtonian gravitational constant and ρ is the density of matter. For example, in the case of a point mass of magnitude M at a displacement r, i.e. $\rho = M\delta(\boldsymbol{r})$, the potential of the distribution: ϕ is

$$\phi = -G\frac{M}{r}.$$

In 1915, A. Einstein published General Relativity as a theory of the relationship between spacetime and matter [1, 2]. In this theory, we consider 4 dimensional spacetime $x^\mu = (ct, x, y, z)$ as a manifold and we call a coordinate a "world point". The interval between two world points $\mathrm{d}s$ is described as

$$\mathrm{d}s^2 = g_{\mu\nu}\mathrm{d}x^\mu\mathrm{d}x^\nu,$$

where $g_{\mu\nu}$ is a metric tensor.

In general relativity, space, time and matter interact and their relationship is described as

$$G_{\mu\nu} = \frac{8\pi G}{c^4}T_{\mu\nu}, \tag{1.1}$$

where $G_{\mu\nu}$ is the Einstein tensor, which includes the information about spacetime and $T_{\mu\nu}$ is the stress-energy-momentum tensor which includes the information about matter.

In 1916, Einstein predicted the existence of gravitational waves from eq. (1.1) [4]. Gravitational waves are ripples in time-space. In a case of a weak gravitational field, we can use a metric like

$$g_{\mu\nu} = \eta_{\mu\nu} + h_{\mu\nu}, \qquad |h_{\mu\nu}| \ll 1. \tag{1.2}$$

By substituting eq. (1.2) in eq. (1.1), we can get the linearized Einstein equation:

$$\Box h_{\mu\nu} = -\frac{16\pi G}{c^4} T_{\mu\nu}. \tag{1.3}$$

When $T_{\mu\nu} = 0$, eq. (1.3) becomes

$$\Box h_{\mu\nu} = 0, \tag{1.4}$$

whose solution is

$$h_{\mu\nu} = A_{\mu\nu} \exp(i\omega_g(t - z/c)), \tag{1.5}$$

$$A_{\mu\nu} = \begin{pmatrix} 0 & 0 & 0 & 0 \\ 0 & h_+ & h_\times & 0 \\ 0 & h_\times & -h_+ & 0 \\ 0 & 0 & 0 & 0 \end{pmatrix}, \tag{1.6}$$

where ω_g is the angular frequency of the GW and h_+ and $h_\times$ are called the amplitudes of the "plus" and "cross" polarizations of the GW. From eq. (1.5) we see GWs propagate at speed of light and from eq. (1.6) we see they have two independent polarization modes. Fig. 1.1 is an image of "Plus mode" and "Cross mode".

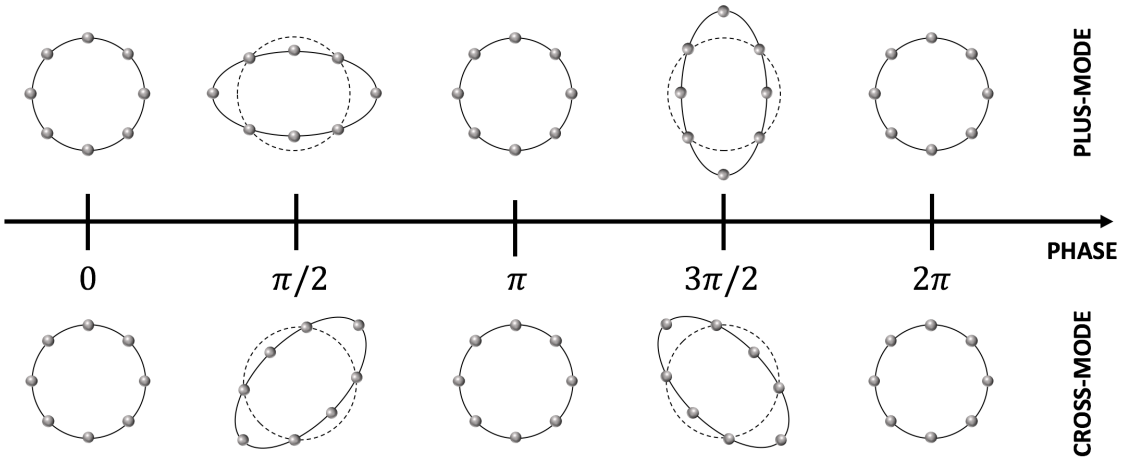

Figure 1.1: Polarization modes of gravitational waves

When a mass accelerates, it emits GWs. Because of the conservation of energy, GWs don't emit a monopole. And because of the conservation of momentum and angular momentum, GWs don't emit a dipole. From the quadrupole approximation, the amplitude of the gravitational wave is calculated as [5]

$$h_{ij} = \frac{2G}{c^4 R} \ddot{Q}_{ij}, \tag{1.7}$$

where R is the distance between the source of gravitational waves and the observer and Q_{ij} is the quadrupole moment of the mass distribution.

1.1.1 Sources of Gravitational Waves

Compact Binary Coalescence (CBC)

Compact Binary Coalescence is an coalescence event like black hole (BH) – BH and neutron star (NS) – NS. Advanced LIGO (aLIGO) first detected GWs from a BH–BH binary beyond ∼400 Mpc [3]. aLIGO and Virgo also detected GWs from a NS–NS binary [**?**]. Up to now, 11 CBC events has been detected [6]. Other strong possibilities are GWs from BH-NS binary [7] but they have not been detected yet. Typical estimated maximum amplitude is $h \sim 10^{-21}$ and estimated frequency before is $f = c^3/(\pi 6^{1.5} GM) \sim 4.4\times10^3/(M/M_\odot)$ Hz, where M is the total mass of CBC and $M_\odot$ is the mass of the sun [9]. In this case, since the wave-form is predicted from Post-Newtonian approximation and numerical simulation, we can use a matched filter which helps to get gravitational wave signal efficiently from noise. With second generation GW detectors: aLIGO, AdVirgo and KAGRA, several or dozens of detections are expected per year [8].

Supernova (SN)

When a supernova occurs, if the core of the star is asymmetric, it produces gravitational waves. Unlike a CBC, it is difficult to predict the waveform of gravitational waves emitted by a supernova explosion. Because of this, we cannot use a matched filter to find a signal from a detector in this case. On the other hand, the frequency of supernova explosions is higher than that for CBCs. The estimated GW frequency is around 1 kHz [10].

Pulsar

A pulsar is a highly magnetized rotating neutron star or white dwarf that emits a beam of electromagnetic radiation [11]. If a pulsar is asymmetric, it emits gravitational waves. Especially, millisecond pulsars whose rotation period are between 1 ms and tens of ms emit gravitational waves whose frequency are between about 10 Hz and 1000 Hz. GWs from pulsars are weaker than those from CBCs.

Others

Other sources are Gamma-Ray Bursts (GRB) source, Low-Mass X-ray Binaries (LMXB), Soft Gamma (-ray) Repeaters (SGR) and the Gravitational Wave Background (GWB). GWs from these sources have not been detected yet. table 1.1 classifies the types of GWs by predictability and duration.

Table 1.1: Type of GWs

Waveform	Short time	Long time
Predictable	CBC, GRB source	pulsar, LMXB
Unpredictable	SN, SGR	GWB

1.1.2 Detection of Gravitational Waves

In 1974, R. A. Hulse and J. H. Taylor proved the existence of gravitational waves indirectly and won Nobel prize in 1993 [12, 13]. They showed that their data fit the equation in fig. 1.2 from General Relativity:

$$\begin{aligned}\dot{P}_b = &-\frac{192\pi G^{5/3}}{5c^5}\left(P_b/2\pi\right)^{-5/3}\left(1-e^2\right)^{-7/2} \\ &\times\left(1+\frac{73}{24}e^2+\frac{37}{96}e^4\right)m_p m_c\left(m_p+m_c\right)^{-1/3},\end{aligned} \tag{1.8}$$

where P_b is the orbital period , e is the eccentricity, m_p is the pulsar mass and m_c is the companion mass.

In 2015, LIGO (Laser Interferometer Gravitational-Wave Observatory) achieved the first direct detection of gravitational waves, which were from the merger of a $36^{+5}_{-4}M_\odot$ BH and a $29^{+4}_{-4}M_\odot$ BH. The final BH mass was $62^{+4}_{-4}M_\odot$, with $3.0^{+0.5}_{-0.5}M_\odot c^2$ radiated in gravitational waves [3]. Fig. 1.3 shows the time series of the amplitudes of the GW. For this achievement, R. Weiss, B. C. Barish and K. S. Thorne won Nobel prize in 2017. Especially interesting is the event GW170817, which was the first detected merger of two neutron stars and the first multi-messenger observation. First GWs were detected and estimated the rough location of the source on the celestial sphere. Using this estimation, many radio telescopes detected the astronomical event.

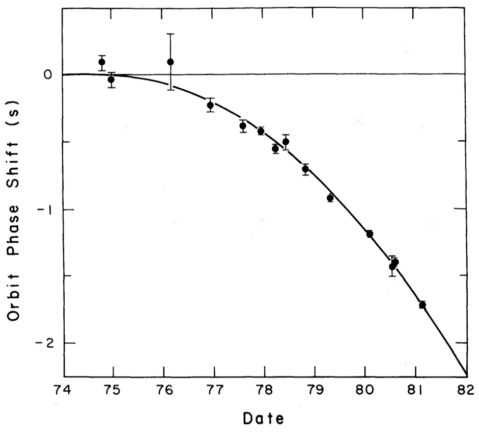

Figure 1.2: Orbital phase residuals. Figure taken from Ref. [13]

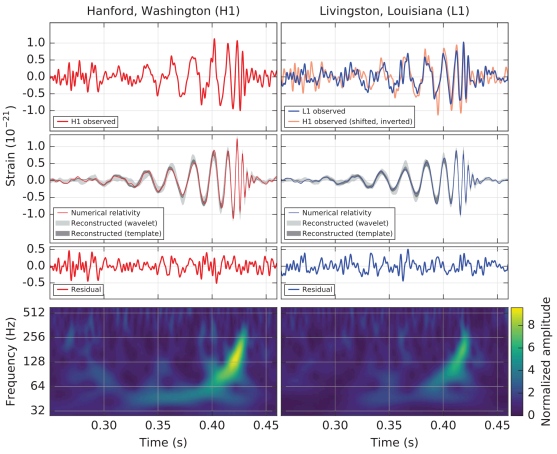

Figure 1.3: LIGO's first direct detection of GWs. Figure taken from Ref. [3]

1.2 Gravitational Waves Telescopes

1.2.1 Resonant Mass Antennas

J. Weber made an attempt at detecting gravitational waves in 1960s [14]. He made a series of resonant mass antennas, nowadays called "Weber bar." The equation of motion

of a Weber bar is

$$\mu\left(\ddot{\xi}+\frac{\omega_0}{Q}\dot{\xi}+\omega_0^2\xi\right)=f_{\mathrm{GW}}(t), \tag{1.9}$$

where μ is the Lamé parameter, ω_0 is the normal frequency, ξ is a distance between arbitary two points in the bar, Q is the mechanical quality factor and f_{GW} is the tidal power from the GW [15]. When a GW whose frequency is very close to the resonant frequency of the bar passes by, the bar oscillates in a normal mode. However he never observed GWs.

1.2.2 Interferometeric Detectors

Because of the resonant mass antennas' narrow observable frequency band, a laser interferometric detector is mainstream in these days. Here is an image of a Michelson interferometer with the mirrors suspended by wires in fig. 1.4. The principle of the de-

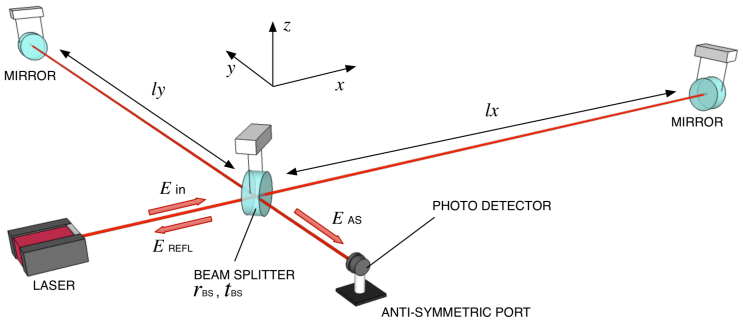

Figure 1.4: A Michelson Interferometer. Figure taken from Ref. [16]

tection of GWs is as follow. An incoming coherent beam is split at Beam Splitter (BS), one beam passes straight and the other beam turns 90 degrees. Both beams are reflected by the end mirrors, go through the BS again and thence to the entrance port and a photo detector. When GWs pass the interferometer, the arm lengths change as

$$\begin{pmatrix}\Delta l^x\\ \Delta l^y\end{pmatrix}=\frac{1}{2}h_+\begin{pmatrix}l^x\\ l^y\end{pmatrix}e^{i\omega_{\mathrm{g}}(t-z/c)}+\frac{1}{2}h_\times\begin{pmatrix}l^y\\ l^x\end{pmatrix}e^{i\omega_{\mathrm{g}}(t-z/c)}, \tag{1.10}$$

and we can get the GWs information from the change of the laser's phase at the photo detector. The frequency response function from GWs to the Michelson interferometer is

$$H_{\mathrm{MI}}(\omega_{\mathrm{g}})=\frac{2\Omega\sin\gamma}{\omega_{\mathrm{g}}}e^{-i\gamma}, \tag{1.11}$$

$$\gamma=\frac{l\omega_{\mathrm{g}}}{c} \tag{1.12}$$

and when

$$\gamma=\frac{\pi}{2} \tag{1.13}$$

satisfied, in other words when $\omega_{\rm g} \simeq 100$ Hz and $l_x = l_y \simeq 750$ km for example, $|H_{\rm MI}(\omega_{\rm g})|$ is maximized. However it is impossible to build a 750 km arm length interferometer for the Earth is a sphere. There are two main solutions to this problem: using Fabry-Pérot cavities and delay lines in the arms. Here is an image of Fabry-Pérot Michelson interferometer which is shown in fig. 1.5. To increse the optical path length, we set a

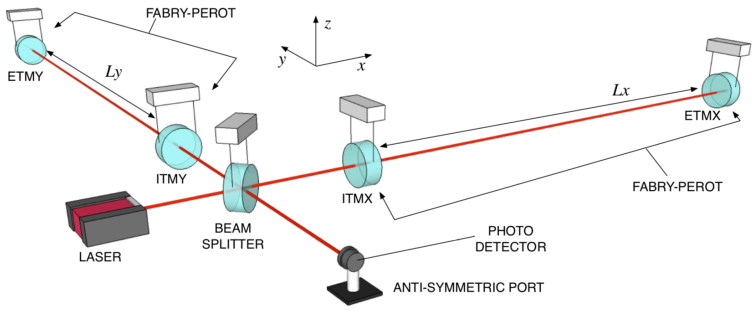

Figure 1.5: A Fabry-Pérot (FP) Michelson Interferometer. Figure taken from Ref. [16]

mirror between the BS and the end mirror. Then, the beam reflects and makes many round trips and creates a longer effective arm length interferometer. The frequency response function of a FP Michelson interferometer is

$$H_{\rm FPMI}(\omega_{\rm g}) = \frac{\alpha}{1 - r_{\rm F} r_{\rm E} e^{-2i\gamma}} H_{\rm MI}(\omega_g), \tag{1.14}$$

$$\alpha = \frac{t_{\rm F}^2 r_{\rm E}}{-r_{\rm F} + (r_{\rm F}^2 + t_{\rm F}^2)\, r_{\rm E}}, \tag{1.15}$$

where Ω is the angular frequency of the laser, $r_{\rm F}$ is the reflectance of the FP cavity's front mirror, $r_{\rm E}$ is the reflectance of the FP cavity's end mirror, and $t_{\rm F}$ is the transmittance of the FP cavity's front mirror.

Furthermore, to recycle the laser beams which head to the beam port and the photo detector, we set Power Recycling mirrors and Signal Recycling mirrors. The principle is from an application of Michelson interferometer. Fig. 1.6 is an applied version of Michelson interferometer: a Dual-Recycled Fabry-Pérot Michelson Interferometer.

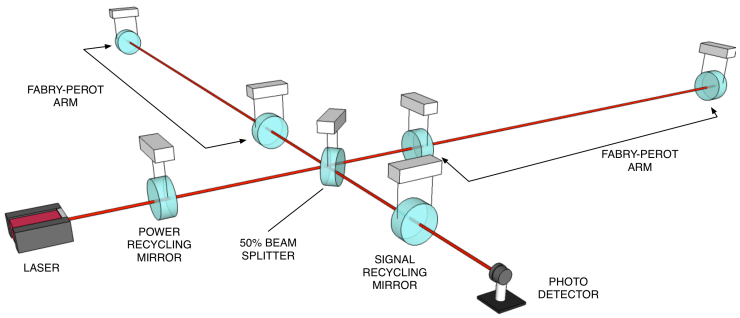

Figure 1.6: A Dual-Recycled Fabry-Pérot (DRFP) Michelson Interferometer. Figure taken from Ref. [16]

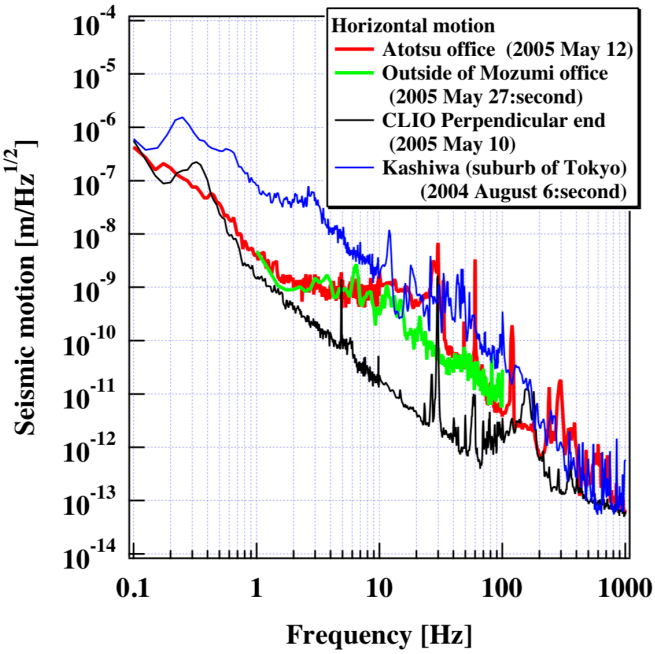

Figure 1.7: Typical measured seismic motion of outside of Kamioka mine. Figure taken from Ref. [17]

1.2.3 Noise source

Seismic Noise

Except duaring an earthquake, in everyday life we seldom feel ground vibrations; however it always vibrates with very small amplitudes. Because of this, when one builds an interferometer on ground, one cannot avoid an effect from seismic noise. It is well known that seismic spectrum is roughly proportional to f^{-2}. In fact, the power spectrum in Kamioka [17] which is shown in fig. 1.7 is more or less described as

$$x_{\rm seis} = \frac{10^{-9}}{f^2}\ {\rm m}/\sqrt{\rm Hz} \quad f \geq 0.1\ {\rm Hz}. \tag{1.16}$$

Because the seismic motion is larger than the requirement of KAGRA, we need the vibration isolation system.

Thermal Noise

Since an interferometer is always in contact with a finite-temperature thermal reservoir, the component always vibrate thermally. Especially, the vibration of mirrors (both mirror part and coating part) changes the optical path length, so we need to reduce this [18]. Thermal noise is generally described by the Fluctuation Dissipation Theorem. There are two kinds of damping, one is a viscous damping and the other is structural damping. The viscous damping is from residual gas in a chamber and its spring constant is real number. On the other hand, the structural damping is related with the internal structure of the suspension and its spring constant is complex number. When we have a viscous damping,

the power spectrum of thermal noise is described by [19]

$$G_x(\omega) = \frac{4k_BT}{mQ}\frac{\omega_0}{\left(\omega^2-\omega_0^2\right)^2+\omega_0^2\omega^2/Q^2}, \tag{1.17}$$

$$G_x(\omega) \simeq \frac{4k_{\mathrm{B}}T}{m\omega_0^3Q} \propto f^0 \quad (\omega \ll \omega_0), \tag{1.18}$$

$$G_x(\omega) \simeq \frac{4\omega_0 k_{\mathrm{B}}T}{m\omega^4Q} \propto f^{-4} \quad (\omega \gg \omega_0), \tag{1.19}$$

$$f = 2\pi\omega, \tag{1.20}$$

where k_{B} is Boltzmann's constant, T is temperature, m is the mass of the component, Q is Q factor, ω_0 is the resonance angular frequency. On the other hand, when we have structural damping, the power spectrum of thermal noise is

$$G_x(\omega) = \frac{4k_BT}{mQ\omega}\frac{\omega_0^2}{\left(\omega^2-\omega_0^2\right)^2+\omega_0^4/Q^2}, \tag{1.21}$$

$$G_x(\omega) \simeq \frac{4k_BT}{m\omega_0^2Q}\frac{1}{\omega} \propto f^{-1} \quad (\omega \ll \omega_0, Q \gg 1), \tag{1.22}$$

$$G_x(\omega) \simeq \frac{4k_BT\omega_0^2}{mQ}\frac{1}{\omega^5} \propto f^{-5} \quad (\omega \gg \omega_0, Q \gg 1). \tag{1.23}$$

Laser Noise

There are many kinds of laser noises: frequency noise, scattering noise, radiation pressure noise and intensity noise. The most problematic noise is the frequency noise. When the phase difference is $\delta\nu(\omega)$ in a Fabry-Pérot cavity, the noise is [20]

$$\delta\phi^{(\mathrm{F})}_{\mathrm{FPMI}} = \epsilon_{\mathrm{CMRR}}\int_{-\infty}^{\infty} H^{(\mathrm{F})}_{\mathrm{FP}}(\omega)\delta\nu(\omega)e^{i\omega t}\mathrm{d}\omega, \tag{1.24}$$

where ϵ_{CMRR} is the Common Mode noise Rejection Ratio. To stabilize the frequency, it is common to use another Fabry-Pérot as a frequency reference device. However, since the main interferometer itself is most sensitive to the frequency noise, we can also use it to feedback its signal as well.

Gas Noise

Since molecules in the air have some finite size, the higher the number density, the more the laser is scattered. Furthermore, when there are molecules on the optical path, the refractive index changes and as a result, the optical path length changes. The mean square of the optical pass length difference noise is described as [21]

$$\left\langle \delta x^2 \right\rangle \propto n \propto \frac{p}{k_BT_{\mathrm{gas}}}, \tag{1.25}$$

$$\left\langle \delta x^2 \right\rangle = 4\sqrt{2}\pi\alpha^2 m_{\mathrm{mol}}^{1/2}\int_0^L \frac{p\left(z\right)}{r_{\mathrm{laser}}\left(z\right)\left\{k_{\mathrm{B}}T_{\mathrm{gas}}\left(z\right)\right\}3/2}\mathrm{d}z, \tag{1.26}$$

where n is the number density, p is the pressure, $T_{\rm gas}$ is the temperature of the gas, α is the polarizability of the molecule, $m_{\rm mol}$ is the mass of the molecule, L is the baseline length of the interferometer, and $r_{\rm laser}$ is the radius of the laser. To prevent this, the pressure in a duct in KAGRA is kept at 10^{-7} Pa.

1.2.4 Interferometric Detector Projects

The development of laser interferometric gravitational wave detectors started in the early 1970s [22, 23]. At first, several groups tried to build interferometric detectors a few dozen meters in length. As of now there are three km-class interferometer detectors. Table 1.2 summarizes GW detectors around the world.

Table 1.2: Project

Project	Baseline length	Type	state
aLIGO[1]	4 km	ground	online
AdVirgo	3 km	ground	online
KAGRA	3 km	ground	under construction
GEO600	600 m	ground	online
TAMA300	300m	ground	built but offline
Einstein Telescope	10 km [24]	ground	under study
Cosmic Explorer	40 km [25]	ground	under study
LISA	2,500,000 km	space	under construction
DECIGO	1,000 km	space	under study

1.2.5 KAGRA

KAGRA is an interferometric detector which is under construction in Japan. It is designed to detect the coalescence signal of binary NS at a distance of ∼250 Mpc with SNR=10 when the sources are at the optimal orientation with respect to KAGRA at the time of the event [26]. There are two characteristics of KAGRA. One is that it is constructed underground. This is because the seismic noise underground is 10^{-2} times smaller than ground noise in range 1 – 100 Hz [17]. The other is that four key mirrors (two front mirrors and two end mirrors) are cryogenic. Here is the target sensitivity of bKAGRA in fig. 1.8.

[1] In the USA, there are two gravitational wave detectors: LIGO(Hanford) and LIGO(Livingstone).

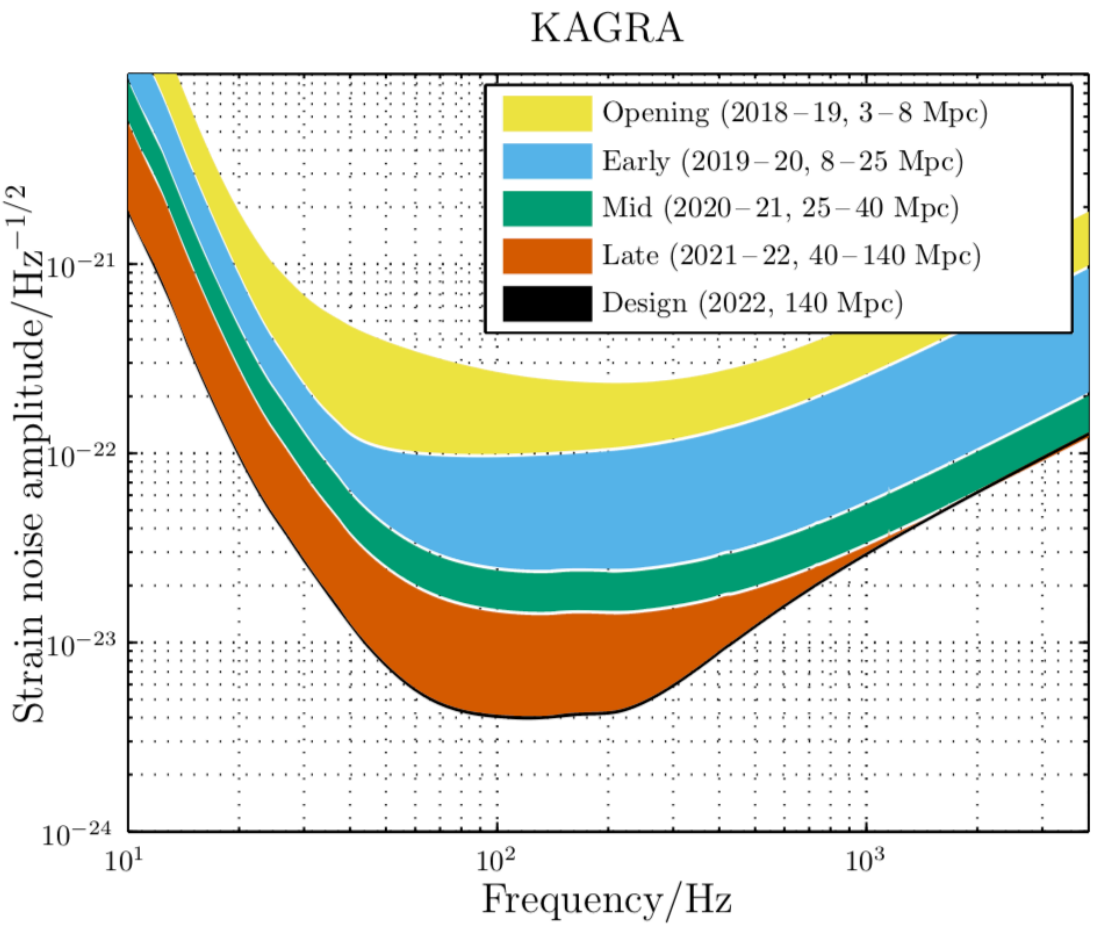

Figure 1.8: Target sensitivity curves of KAGRA. Taken from [27]

2 Vibration Isolation System for KAGRA

2.1 Vibration isolation Pendulum

2.1.1 Vibration Isolation due to a Pendulum

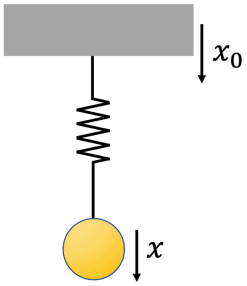

Figure 2.1: Spring pendulum

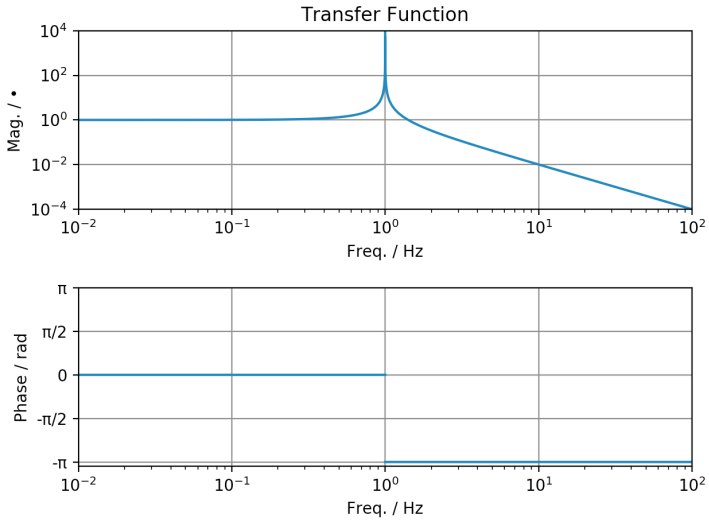

Figure 2.2: Spring pendulum

In order to isolate a system from seismic vibration, one can use mechanical filter with elastic components, such as springs and pendulums. To understand how the mechanical filter works, let us consider a simple example, a dimensional spring with a mass attached as shown in fig. 2.1. The equation of motion of this system is,

$$m\ddot{x} = -k(x - x_0), \tag{2.1}$$

where m is the mass of the pendulum, x is the position of the mass, x_0 is the ground position and k is a spring constant. Note that both x and x_0 are time-dependent variables. By the Fourier transform of this equation of motion and adjusting the appropriate constants, we can get the transfer function of this pendulum,

$$H(f) := \frac{\tilde{x}(f)}{\tilde{x}_0(f)} = \frac{1}{1 - f^2}, \tag{2.2}$$

where $f_0 = 2\pi\sqrt{k/m}$ is the resonant frequency. Fig. 2.2 shows the Transfer function of eq. (2.2) where $f_0 = 1$ Hz. When the frequency is much lower than the resonant frequency, $f \ll f_0$, $H(f)$ is a constant, and when the frequency is much higher than the resonant frequency, $f \gg f_0$, the magnitude of $H(f)$ rolls off proportionally to f^{-2}. From these characteristics, we can reduce the vibration. On the other hand, when $f \simeq f_0$, the motion of the mass is amplified exceedingly.

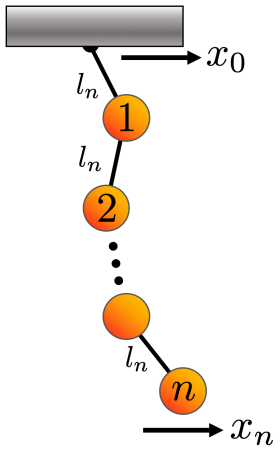

Figure 2.3: n stages pendulum

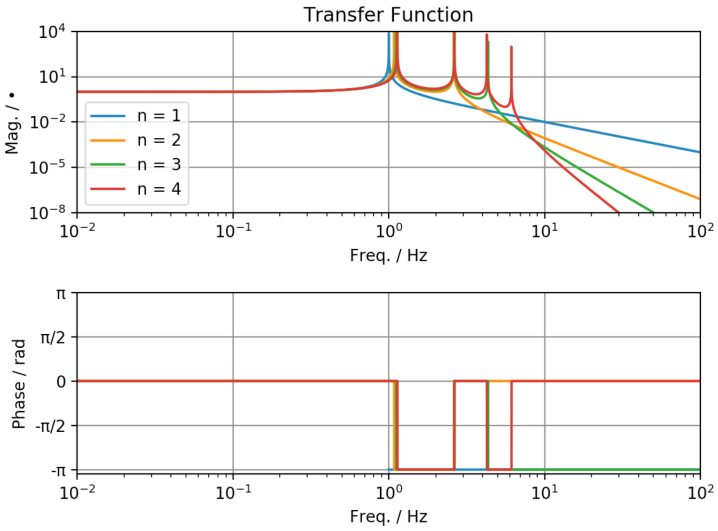

Figure 2.4: TF of n stages pendulum

A n stages pendulum has n resonant frequencies and when the frequency is larger than the maximum resonant frequency, the magnitude of $H_n(f)$ decreases in proportion to f^{-2n} (See fig. 2.3 and fig. 2.4).

2.1.2 Passive Damping

Pendulum reduces the vibration only when $f \gg f_0$. On the contrary, the amplitude is amplified in the vicinity of the resonance frequency. By using a damping filter, one can reduce the magnitude of the test mass around resonant frequency. The easiest example is to consider the velocity term in a pendulum. There are mainly two damping system, one is "Passive Damping" and the other is "Active Damping".

Fig. 2.5 is a damped pendulum and its EOM is

$$m\ddot{x} = -k(x - x_0) - \gamma(\dot{x} - \dot{x}_0), \tag{2.3}$$

where γ is the damping coefficient of the damper. The TF of eq. (2.3) is

$$H(\omega) = \frac{1 + 2i\eta\,(\omega/\omega_0)}{1 + 2i\eta\,(\omega/\omega_0) - (\omega/\omega_0)^2}, \tag{2.4}$$

$$\eta = \gamma/2m\omega_0, \tag{2.5}$$

$$\omega = 2\pi f, \tag{2.6}$$

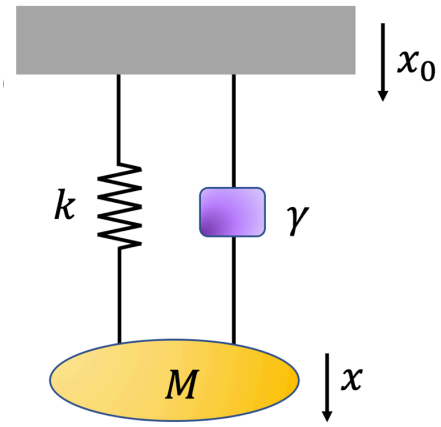

Figure 2.5: viscous damped spring pendulum

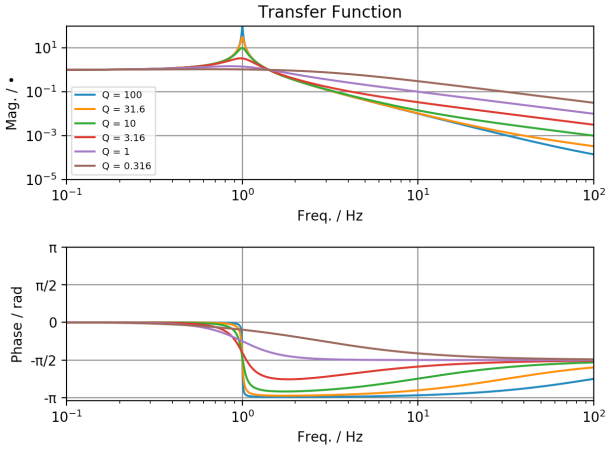

Figure 2.6: Transfer function of viscous damped spring pendulum. When Q is larger, the peak of the transfer function becomes shaper and the magnitude at high frequency is lower.

where η is the damping ratio, ω is the angular frequency. A quality factor of the resonance below is a good parameter to check the characteristics of the pendulum,

$$Q = \frac{1}{2\eta}, \tag{2.7}$$

and fig. 2.6 shows the transfer function of the pendulum at each Q. When the frequency is higher than Qf_0, the magnitude decreases in proportion to f^{-1}.

The other passive damping which is called "flexible damping", is to use the other spring and mass in fig. 2.7. With flexible damper, one can decrease the magnitude in proportion to f^{-2} without poles. Table 2.1 is a table of characteristics of damping.

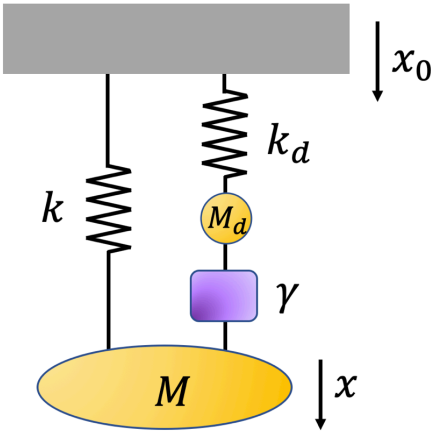

Figure 2.7: flexible damped spring pendulum

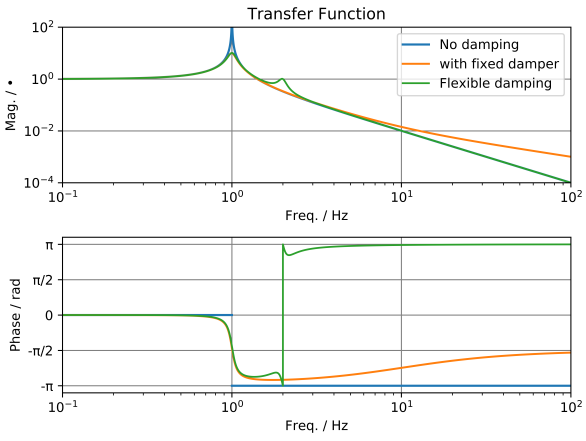

Figure 2.8: TF of flexible damping

An example of passive damping is an eddy current damping system which is used in KAGRA as well. Eddy currents are loops of electrical current induced within conductors

Table 2.1: characteristics of suspenson

Type	No damping	Fixed damping	Flexible damping
magnitude at high freq.	$\propto f^{-2}$	$\propto f^{-1}$	$\propto f^{-2}$

by a changing magnetic field in the conductor due to Faraday's law of induction. For instance, when a permanent magnet moves parallel to a metal plate like aluminum and copper, the relative velocity between the magnet and metal plate decrease.

2.1.3 Active Damping

Passive damping filter like an eddy current damper's performance depends on the relative velocity of the magnet, that is it depends on the frequency of the suspended masses. Since multi stages suspensions have many different resonant frequency, a passive damping is not universal for damping systems. Furthermore, suspension systems with eddy current dampers suffer from severe thermal noise at high frequencies, therefore it is completely impossible to use them near the optics. In that case, one can use "active damping".

In active damping, one can use feedback signals to damp the systems. Thanks to this damping, one can control the frequency response and tune flexibly by designing servo filters. So when one has set enough amount of sensors and actuators, it is possible to control the system in all translational and rotational degrees of freedom. In other words, the quality of servo filters is the key of active damping. If the servo filter is designed insufficiently, it would not send the correct signals to actuators, sensors and electric circuits. That's why one needs to be careful when we design servos.

2.2 Suspension system in KAGRA

In KAGRA, there are mainly three kinds of suspensions. These three kinds of suspensions are for the large optics. There are smaller optics with smaller suspensions. Fig. 2.9 shows the sketch of KAGRA and fig. 2.10 shows the sketch of suspensions. One is called "type A suspension", another is called "type B suspension" and the other is called "type Bp suspension".

Four type A suspensions are installed as Fabry-Pérot cavities and they consist of "type A tower" for vibration isolation and "cryogenic payload" for cooling the mirrors. Since the required sensitivity of input mirrors and end mirrors in fig. 2.11 are 10^{-3} times smaller than that of type B suspension, type A suspension has 5 GAS filters and its total height is 13.5 m. GAS' s details are written in subsection 2.2.2.

Type B suspensions are used for the beam splitter and the signal recycling mirrors. Details are in subsection 2.2.1. Type Bp suspensions are smaller versions of type B suspensions[1] and installed as power recycling mirrors. Table 2.2 shows the basic specifications of suspensions.

[1]Type Bp's "p" is from "prime".

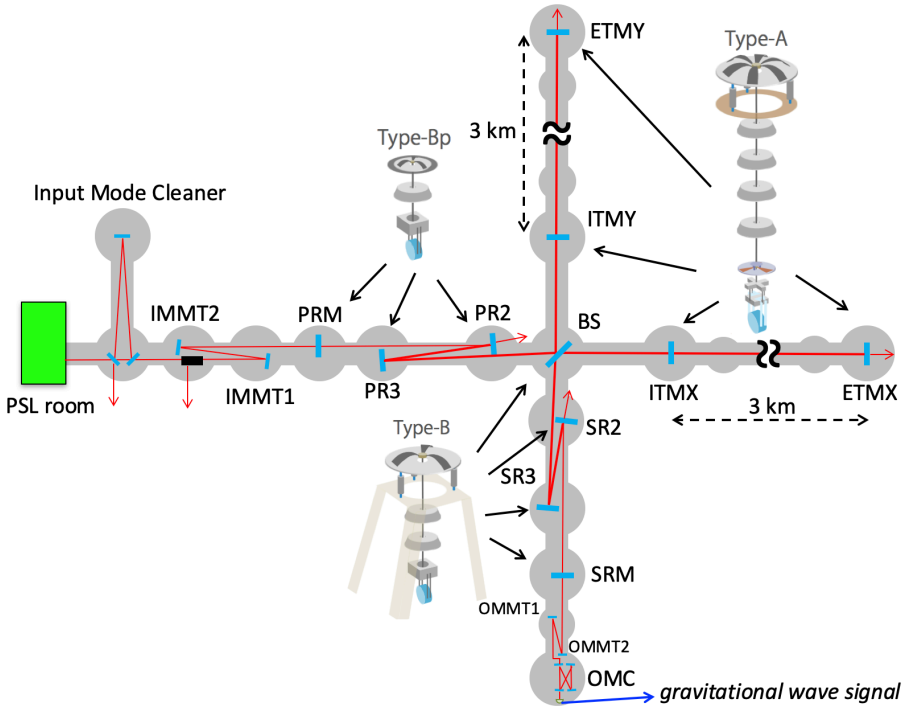

Figure 2.9: Sketch of KAGRA [28]

Table 2.2: Suspensions in KAGRA

	Type A	Type B	Type Bp
Suspended Optics	TM	BS, SRM, SR2, SR3	PRM, PR2, PR3
Number of horizontal stages	9 (included IP)	5 (included IP)	3
Number of vertical stages	6	3	2
Payload temperature	cryogenic (∼20 K)	room temperature	room temperature

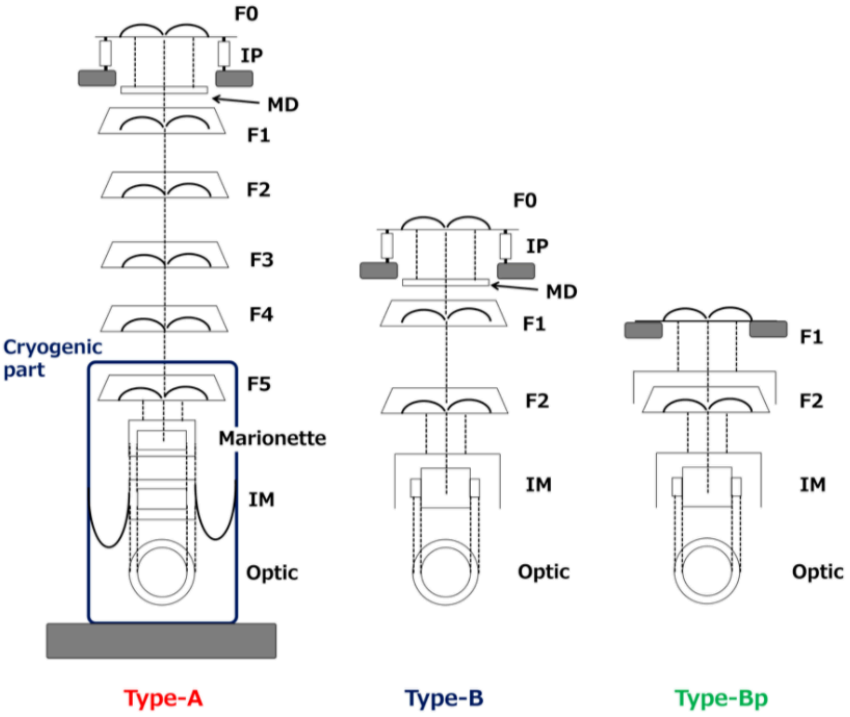

Figure 2.10: Sketch of Suspensions [29].

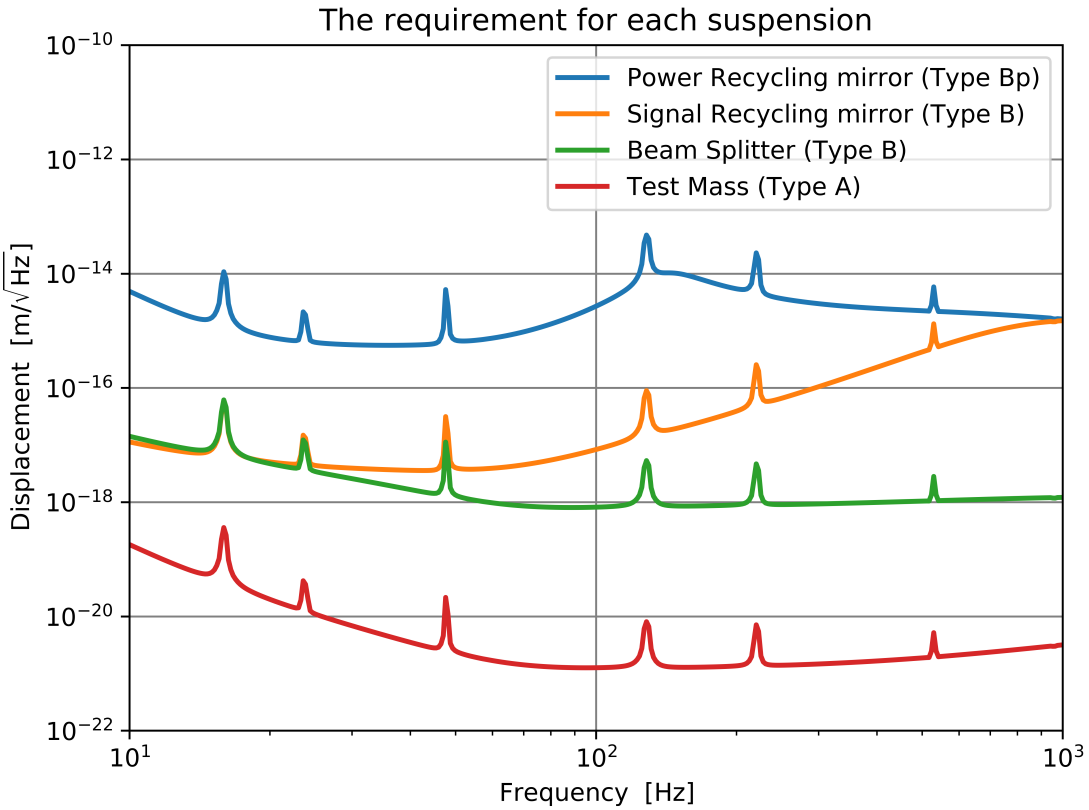

Figure 2.11: Requirement of each suspension. Data is from [**?**].

2.2.1 Overview of Type B suspension

Fig. 2.12 shows the structure of SR3 suspension. In KAGRA, there are one BS and three SRs (SR3, SR2 and SRM). Fig. 2.23 and fig. 2.24 are CAD figures of BS and SRs in KAGRA. A Type B suspension is configured from a payload, GAS Filter chain and Pre-isolator. A payload is configured from Test Mass [2] (TM), Recoil Mass(RM), Intermediate Mass (IM), Intermediate Recoil Mass (IRM) [See subsection 2.2.2]. GAS Filter chain is configured from Bottom Filter (BF) and Standard Filter (SF) [See subsection 2.2.2]. Pre-isolator (PI) is configured from Inverted Pendulums (IP) and Top Filter (TF) [See subsection 2.2.2 and subsection 2.2.2].

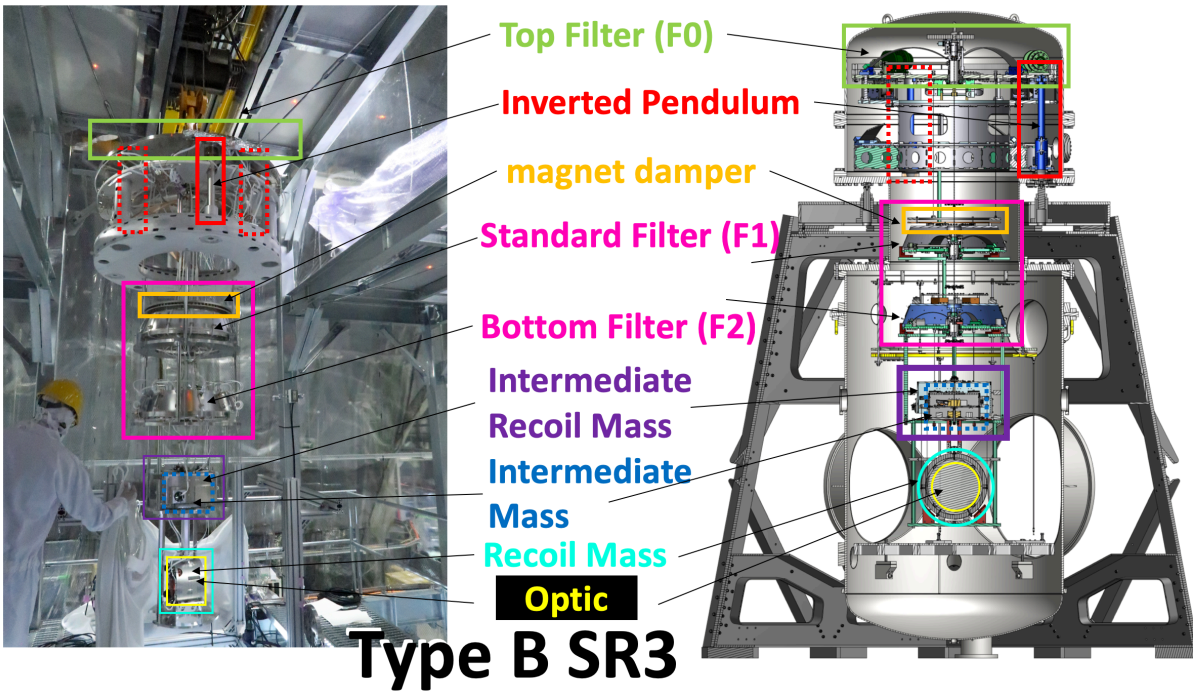

Figure 2.12: Details about SR3 suspension.

2.2.2 Configuration of Type B pendulum

Inverted Pendulum

Pre-isolator in fig. 2.13 comprises an inverted pendulum (IP) with three legs and a GAS filter. IPs support the suspension and it is the only object touching the ground. They reduce the amplitude of seismic vibration at the microseismic peak frequency (0.2-0.5 Hz). Fig. 2.14 describes a typical simple inverted pendulum and the effective spring constant is described as

$$k_{\text{eff}} = \frac{k_\theta}{L^2} - \frac{Mg}{L} \tag{2.8}$$

[2] In general we should call TM only to the masses sensitive to GWs. However, in this thesis we call the other mirrors as TM as well.

where k_θ is the spring constant of the flexure, M is the mass of the load and L is the length of the leg. Usually, the weight of the leg, m, is negligibly small and the following expression, $m \ll M$, holds When $M \ll M_c$, the IP is stable and the resonant frequency is

$$\omega_0 = \sqrt{\frac{g}{L}\frac{M_c - M}{M}}, \tag{2.9}$$

$$M_c = k_\theta / gL, \tag{2.10}$$

where M_c is the critical mass.

The transfer function from the ground displacement to the payload displacement is [29]

$$H_{\mathrm{IP}}(\omega) = \frac{A + B\omega^2}{A - \omega^2}, \tag{2.11}$$

$$A = \frac{k_{\mathrm{eff}}}{M + \frac{m}{4} + \frac{I}{L^2}}, \tag{2.12}$$

$$B = \frac{\frac{m}{4} - \frac{I}{L^2}}{M + \frac{m}{4} + \frac{I}{L^2}}, \tag{2.13}$$

where I is the moment of inertia about the center of mass of IP leg.

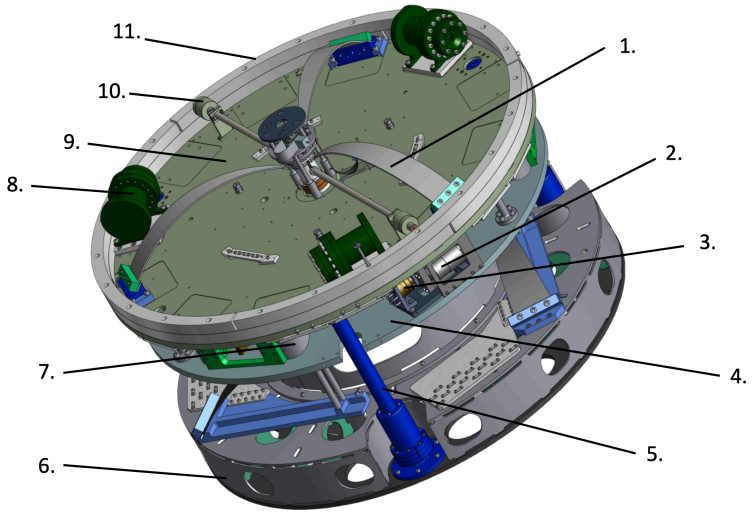

Figure 2.13: CAD Sketch of Pre-Isolator. 1) The top filter for vertical isolation, 2) the coil-magnet actuator, 3) the Linear Variable Differential Transducer (LVDT), 4) the coil support frame rigidly connected to the base ring, 5) the Inverted Pendulum (IP) leg, 6) the base ring, 7) the motorized spring for the static position control of the top stage, 8) thegeophone 9) the top stage isolated by the IP, 10) the magic-wand for compensating CoP effect and 11) the arc–weight.

Geometric Anti Spring

To detect the GWs, one needs to design the suspension which can achieve vertical attenuation performance comparable to that obtainable in the horizontal direction. In order to

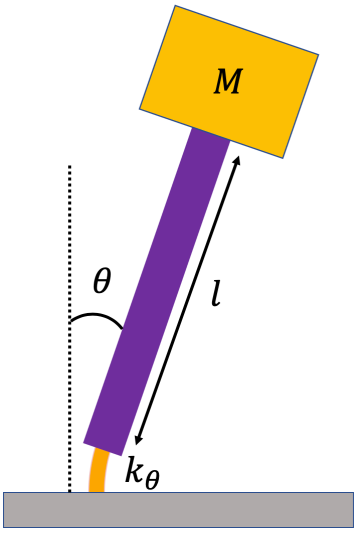

Figure 2.14: Sketch of Inverted pendulum.

achieve this, one must create a spring that satisfies the following requirements. The spring constant must be small on the other hand, the spring must support a heavy mass around hundreds of kilograms. The geometric anti spring (GAS) filter fulfills the requirement and consists of a set of radially-arranged cantilever blades clamped on the base frame and to the central disk called the keystone. The blade were flat when it was manufactured [29]. The other solution to the requirement is to use magnetic anti spring [29], which has been implemented in the superattenuator for Virgo.

Fig. 2.16 shows the analytical model of GAS filter. Now, the payload with mass M is suspended by a GAS filter with the horizontal spring constant k_x, the vertical spring constant k_z. The angle between horizontal axis and horizontal vertical is defined as θ in fig. 2.16. Then, the equation of z-axis motion is described as

$$M\ddot{z} = -k_z\left(z - z_{\mathrm{eq}}\right) - k_x\left(l - l_{0x}\right)\sin\theta, \tag{2.14}$$

where z_{eq} is the equilibrium point, l is the actual length of the horizontal spring and l_{0x} is its natural length. From the Taylor expansion around equilibrium point, z_{eq}, one can get the linearized equation,

$$M\ddot{z} = -\left[k_z - \left(\frac{l_{0x}}{x_0} - 1\right)k_x\right]\left(z - z_{\mathrm{eq}}\right) = -k_{\mathrm{eff}}\left(z - z_{\mathrm{eq}}\right) \tag{2.15}$$

where x_0 is the horizontal distance between the central keystone and the support point of the horizontal spring. From this, the resonant frequency is described as

$$\omega_0 = \sqrt{\frac{k_{\mathrm{eff}}}{M}} \tag{2.16}$$

and this means the resonant frequency depends on the mass of the payload and we can control the resonant frequency with ballast masses. Ballast mass is an additional mass which helps to provide stability to a structure.

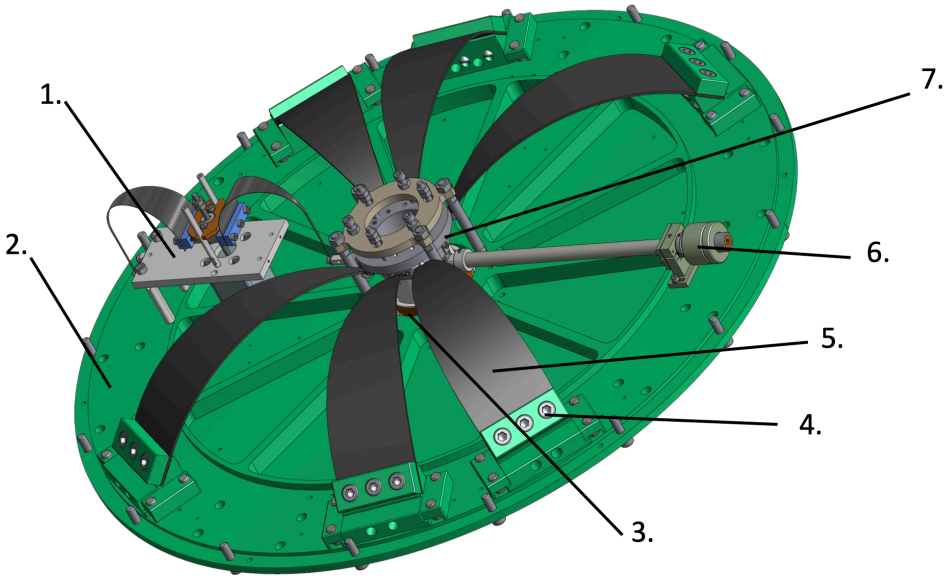

Figure 2.15: CAD Sketch of Geometric anti-spring Filter. 1) The motorized spring for initial positioning of the keystone (fishing rod / FR), 2) the baseplate, 3) the LVDT to monitor the displacement of the keystone, 4) the base clamp, 5) the cantilever blade, 6) the magic-wand for compensating CoP effect and 7) the keystone.

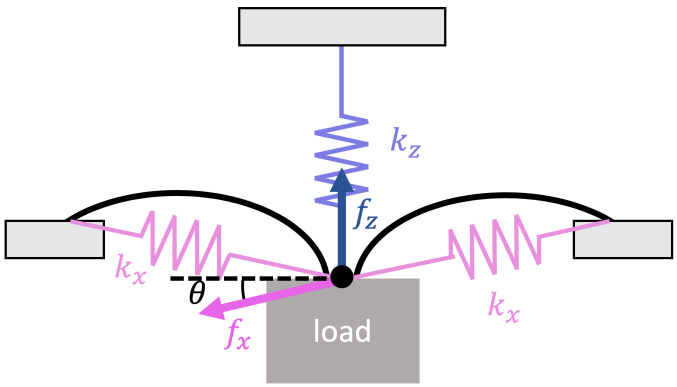

Figure 2.16: An analytical model of the GAS filter.

The system becomes more sensitive to the temperature change as the resonant frequency is reduced by the anti-spring effect and the displacement, Δz, is described as

$$\Delta z = \frac{g}{E\omega_0^2}\frac{\partial E}{\partial T}\Delta T \tag{2.17}$$

where E is the Young's modulus of the spring material and ΔT is the shift of the temperature [29]. And from this, the temperature in the tunnel should be kept the constant ± 0.05 K.

Magnetic Damper

Fig. 2.17 shows the magnetic damper (MD) which is a structural damping for yaw motion. Suspended permanent magnets and this MD attract by electromagnetic force.

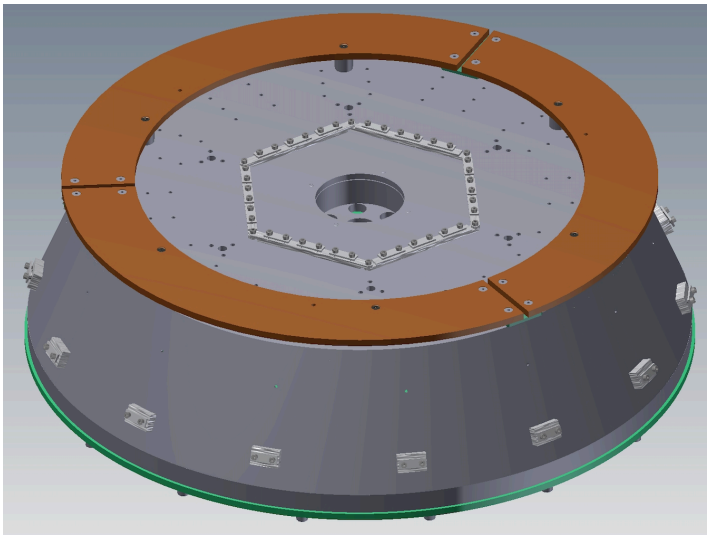

Figure 2.17: Magnet damper rings on a standard filter cap.

Payload

Fig. 2.18 shows the structure of the BS payload. Note the coordinate of the suspension. In this case, longitudinal element is described by z axis. Payload consists of optic, RM, IM and IRM. TM is the main part of suspensions and most important parts. BS and SRs mirrors are made of fused silica. TM is suspended by two piano wires which hold the optic by looping underneath. There are four magnetic protrusions to actuate the optic on its surface [3]. They are controlled by moving them with the RM coil magnet actuators. Because one can not attach a sensor to the TM, one checks its position by using an external device, called Optical Lever (oplev). RM is a hollow cylindrical shape that covers the TM, which is suspended by two tungsten wires.

When one think about the motion of a rigid body, one usually uses "Longitudinal", "Transverse", "Vertical", "Roll", "Pitch" and "Yaw" in fig. 2.19. Usually z axis describes

[3] In the case of BS, the magnets are on the High Reflective (HR) side. On the other hand, in the case of SRs, the magnets are on the Anti- Reflective (AR) side

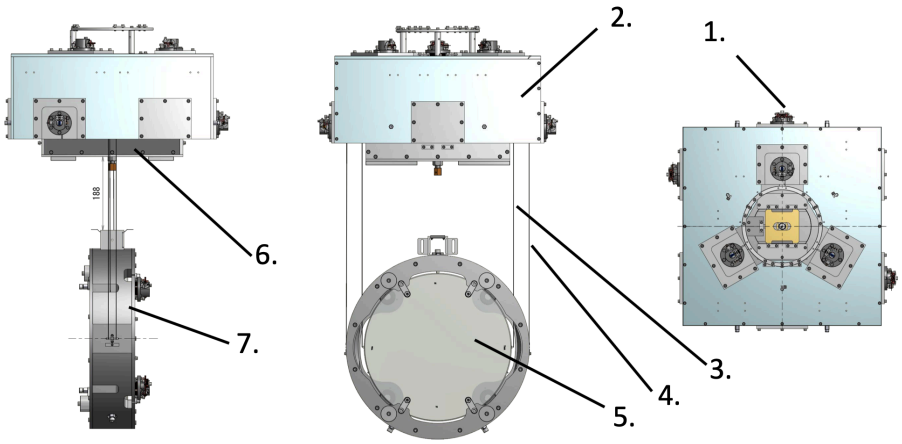

Figure 2.18: CAD pictures of the BS payload. 1) The OSEM unit, 2) the body of the intermediate recoil mass (IRM), 3) the piano wires to suspend the mirror (the optics), 4) the tungsten wires to suspend the recoil mass (RM) of the test mass, 5) the test mass (TM), 6) the body of the intermediate mass (IM) and 7) the body of the recoil mass (RM).

vertical element, but In this model, z axis describe the longitudinal (Beam axis) x axis describes the transverse and y axis describes the vertical in fig. 2.19.

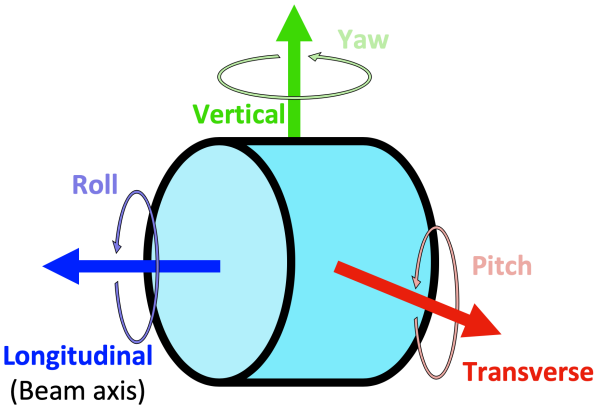

Figure 2.19: coordinate system

The IM is suspended by a single rod from the BF and the IRM is suspended by three rods from the basement of the BF. The shape of the IM is rectangular parallelepiped with two pico motors inside. By using these, delicate positioning and inclination adjustment of IM is done first, but we don't use these to do feedback control. There are 6 Optical Sensor Electro Magnetic-actuator (OSEM) flags in the IM, and one can control the position with the OSEMs in the IRM. The OSEM flag and the OSEM correspond one by one, and there are six in total, three horizontal components and three vertical components. The IRM is shaped like an empty box and is suspended so as to cover the IM from above.

2.2.3 Sensor and actuator

OSEM

The OSEM in fig. 2.20 consists of a LED and a photo detector (PD). When the IM moves, OSEM flags move as well and they change the amount of light that on the PD receives. From calculating this, one can get the position and tilt information of the IM.

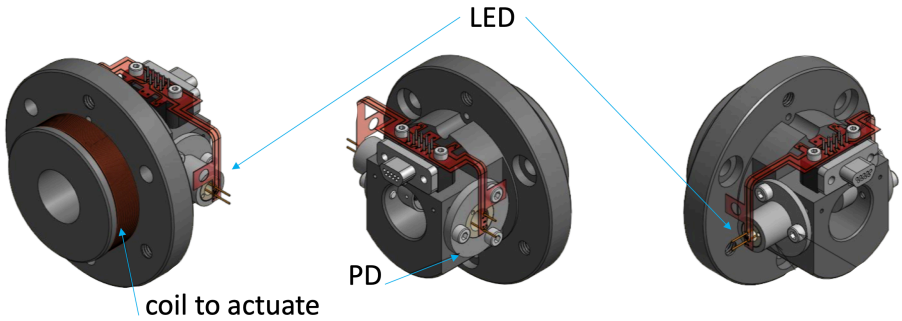

Figure 2.20: CAD pictures of the OSEM

Optical Lever

An Optical lever is a device which detects the displacement of the TM position and its tilt. In case of BS and SRs, the superluminescent diode is injected from the bottom and then reflected by the TM, and finally reaches the quadrant photodiode (QPD) as shown in fig. 2.21. When the mirror moves in longitudinal with displacement d, the beam's horizontal shift is

$$X = 2d \sin \alpha, \tag{2.18}$$

where α is the incident angle on the mirror (See the left figure of fig. 2.22). When the mirror rotates in yaw with angle δ, the angular displacement of the TM, θ is described as

$$\theta = 2\delta \tag{2.19}$$

(See the right figure of fig. 2.22). From this, one can get the relationship between the tilt and position of the mass and the laser shift as

$$\begin{pmatrix} x_f \\ \theta_f \end{pmatrix} = \begin{pmatrix} A & B \\ C & D \end{pmatrix} \begin{pmatrix} x_i \\ \theta_i \end{pmatrix}, \tag{2.20}$$

where the matrix is called "ABCD matrix" and usually the elements are characterized by the focal length and distance between the mirror and the object. Furthermore, we can separate the angle element and the length element theoretically, since no one can put the mirror at 100% correct position, one needs to consider the misplacement. From the comparison of the strength of light on QPDs, one can get the tilt information of the TM.

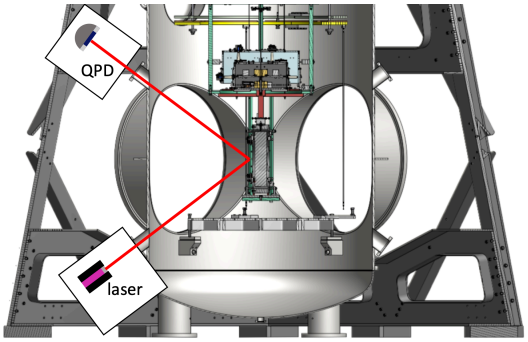

Figure 2.21: Sketch of Oplev

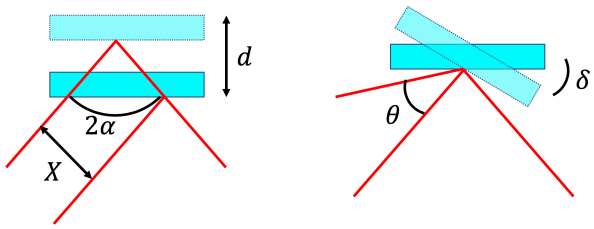

Figure 2.22: Relationship between TM's motion and laser shift.

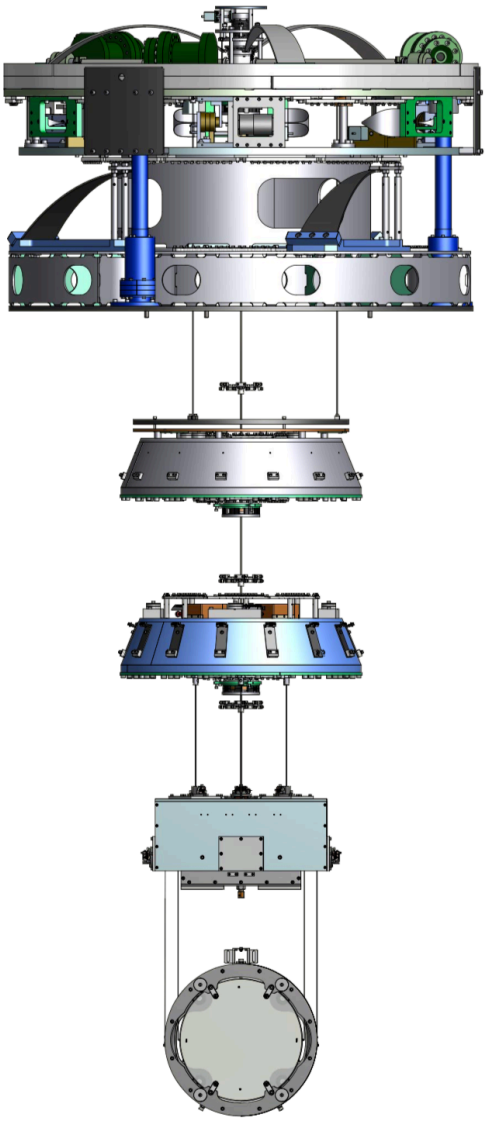

Figure 2.23: Type B suspension for BS.

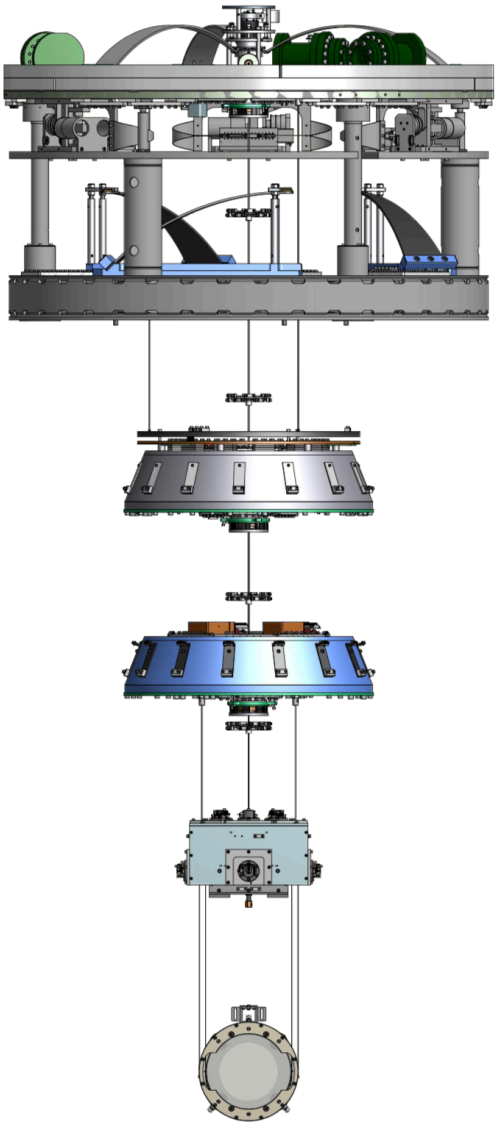

Figure 2.24: Type B suspension for SRs

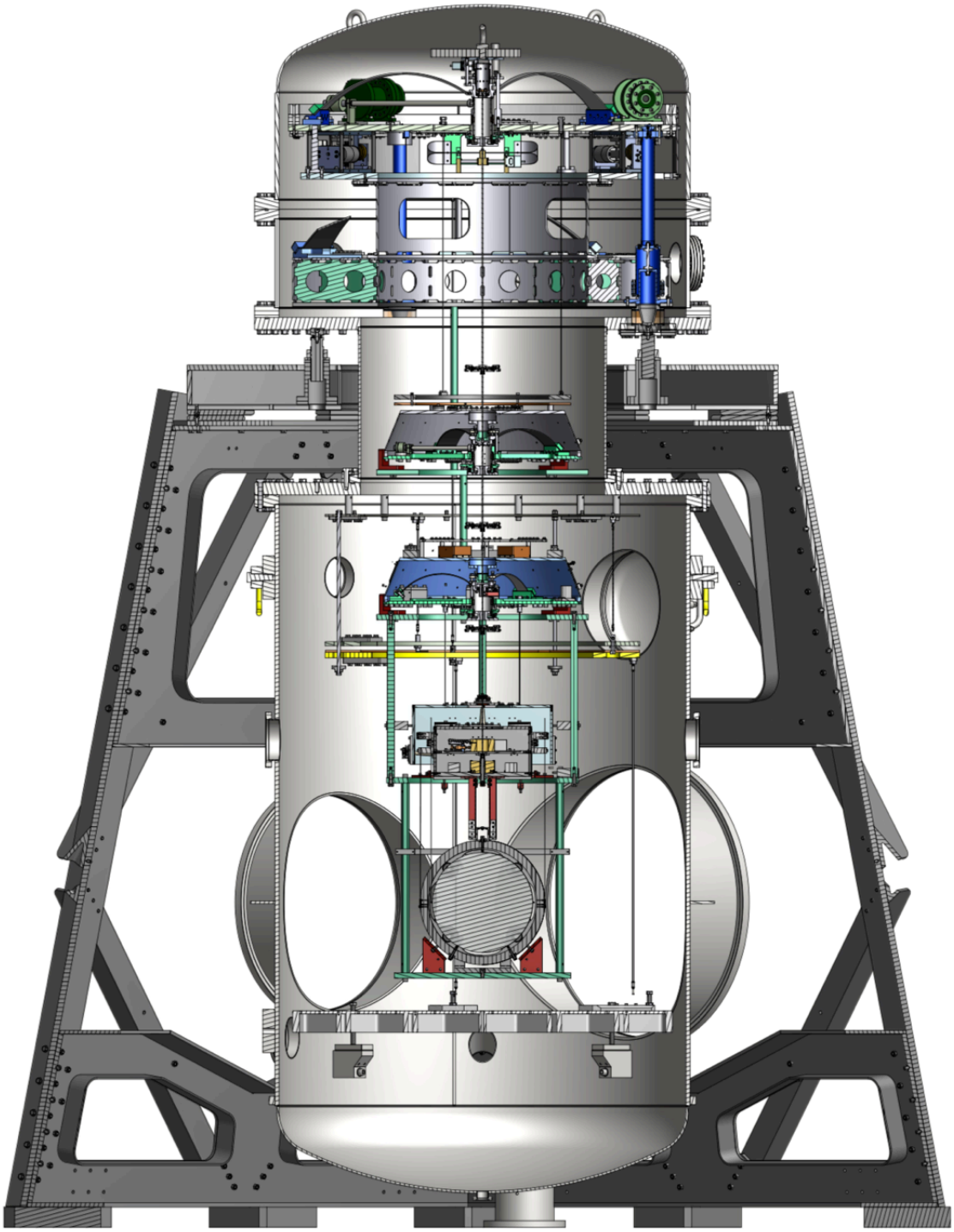

Figure 2.25: Cross section of BS in tank from front (−X, +Y)

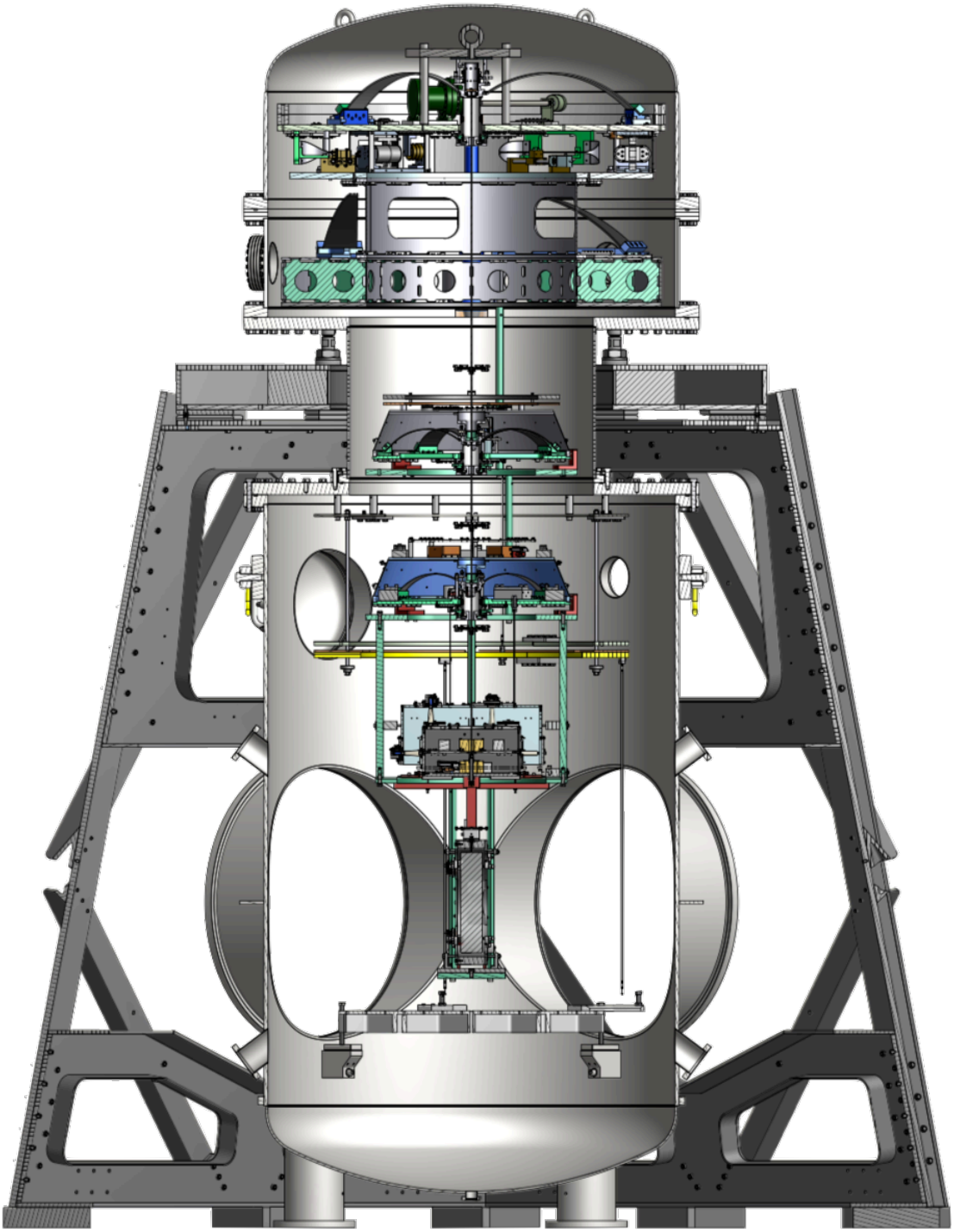

Figure 2.26: Cross section of BS in tank from side (+X, +Y)

3 Suspension model for VIS

3.1 Mathematical Model

3.1.1 Overview

When one wants to control a machine, one needs to build its mechanical model. In case of a suspension, one needs to figure out the equation of motion. In general, there are three kinds of model, this means “point mass model”, “rigid body model” and “elastic body model” in fig. 3.1. A point mass model is used when one does not need to take the shape of the object into account. When one think about the rotation of the Earth for example, one need to consider the shape of the Earth. On the other hand, when one think about the rotation of the Earth around the Sun, one does not need to consider the shape of the Earth and one can regard it as a mass point. This is because the size of the Earth is extremely smaller than that of the Sun. It is also useful for rough estimation of rigid body or elastic body model because it is the simplest and easiest model. A rigid body is a solid body in which deformation is zero or so small it can be neglected. So it includes the information of its direction and its shape is invariant. An elastic body changes its shape due to external force.

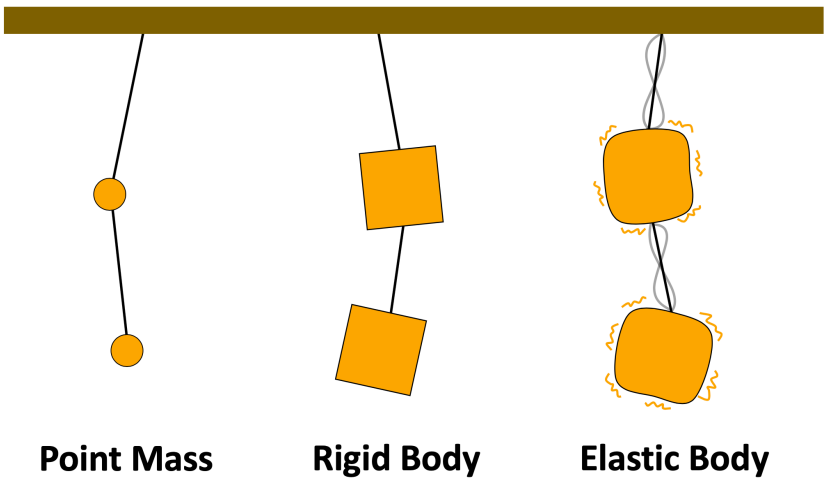

Figure 3.1: Simple diagram of three models.

A suspension model is build from a rigid bodies (orange ones) and elastic bodies (blue

ones) in fig. 3.2. Suspended objects consist of TM, RM, IM, IRM, GAS filter, MD and PI. Suspending objects consist of wires, rods and GAS springs.

The model was build by T. Sekiguchi and here is a list of what the suspension model satisfies [30, 31]

1. All the suspended objects are regarded as rigid bodies with up to 6 DoFs, and their internal elasticity is not taken into account.

2. A wire is assumed to be a massless spring with stretching and torsional elasticity. Since it is assumed to be massless, its violin modes are not taken into account.

3. The vertical spring (GAS filter) used in the model works as an ideal linear spring with a spring constant and a single working-direction. The saturation of the attenuation performance due to center of percussion effect is considered.

4. The dissipation due to the internal friction of the elastic material is taken into account. Thence the spring constants of the vertical springs and wires have imaginary parts with finite loss angles, which are assumed to be constant over all the frequencies (structural damping).

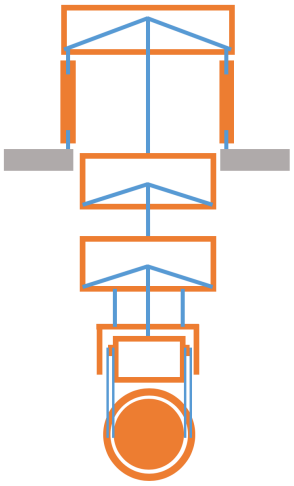

Figure 3.2: Type B suspension model constitution

3.1.2 Coordinate system

The number of degrees of freedom a point mass in a three dimensional space is 3, but in the case of the rigid body is 6 and this includes the position information (eg. x, y, z) and tilt information (eg. $\theta_x, \theta_y, \theta_z$). And now we use the same coordinate definition in subsection 2.2.2.

Translational conversion is commutative conversion on the other hand, Rotation conversion is non-commutative. That means for example, the rotation, in case of rotation around x_i axis and x_j axis ($i \neq j$) has two expressions but they are fundamentally different, $R_{x_i}(\theta_{x_i})R_{x_j}(\theta_{x_j}) \neq R_{x_j}(\theta_{x_j})R_{x_i}(\theta_{x_i})$. In this model, the rotation order is defined like below and image is in fig. 3.3.

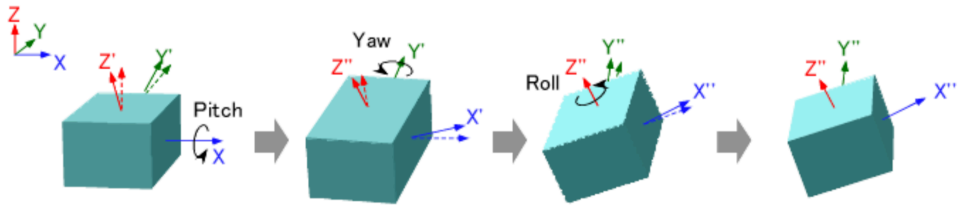

Figure 3.3: the definition of rotation order. 1st. Rotate around x axis. 2nd. rotate around y' axis. 3. rotate around z''. [29]

Since we use wires to hang the objects and wires are clamped on objects, it is convenient to use a local coordinate (x_l, y_l, z_l) which is fixed in the object. And here is the relationship between the global coordinate (x_s, y_s, z_s) and the local coordinate.

$$\begin{pmatrix} x_\mathrm{s} \\ y_\mathrm{s} \\ z_\mathrm{s} \end{pmatrix} = \begin{pmatrix} x \\ y \\ z \end{pmatrix} + \begin{pmatrix} \cos\theta_z & -\sin\theta_z & 0 \\ \sin\theta_z & \cos\theta_z & 0 \\ 0 & 0 & 1 \end{pmatrix} \cdot \tag{3.1}$$

$$\begin{pmatrix} \cos\theta_y & 0 & \sin\theta_y \\ 0 & 1 & 0 \\ -\sin\theta_y & 0 & \cos\theta_y \end{pmatrix} \begin{pmatrix} 1 & 0 & 0 \\ 0 & \cos\theta_x & -\sin\theta_x \\ 0 & \sin\theta_x & \cos\theta_x \end{pmatrix} \begin{pmatrix} x_\mathrm{b} \\ y_\mathrm{b} \\ z_\mathrm{b} \end{pmatrix}, \tag{3.2}$$

where $(x, y, z, \theta_x, \theta_y, \theta_z)$ is the position and the orientation of the suspended object.

3.1.3 Equation of motion of the suspension

One can get the equation of motion from Lagrangian. In case of this suspension, the displacement from the equilibrium point is tiny so one can use the Taylor approximation of Lagrangian, $\mathscr{L}_\mathrm{apr}$ around the equilibrium point, x_eq,

$$\frac{\mathrm{d}}{\mathrm{d}t}\frac{\partial \mathscr{L}_\mathrm{apr}}{\partial \dot{X}} - \frac{\partial \mathscr{L}_\mathrm{apr}}{\partial X} = 0 \tag{3.3}$$

$$\mathscr{L}_\mathrm{apr}(X) = \mathscr{L}(X_\mathrm{eq}) + \left.\frac{\partial \mathscr{L}}{\partial X}\right|_{X=X_\mathrm{eq}} X + \frac{1}{2}\left.\frac{\partial^2 \mathscr{L}}{\partial X^2}\right|_{X=X_\mathrm{eq}} X^2. \tag{3.4}$$

From eq. (3.3), the equation of motion is described as

$$M\ddot{\boldsymbol{x}} + C\dot{\boldsymbol{x}} + K(\boldsymbol{x} - \boldsymbol{x}_\mathrm{eq}) = 0 \tag{3.5}$$

$$M = (M_{ij}) = \left(\left.\frac{\partial^2 T(x, \dot{x})}{\partial \dot{x}_i \partial \dot{x}_j}\right|_{x=x_\mathrm{eq}} \right) \tag{3.6}$$

$$C = (C_{ij}) = \left(\left.\frac{\partial^2 \mathscr{F}(x, \dot{x})}{\partial x_i \partial x_j}\right|_{x=x_\mathrm{eq}} \right) \tag{3.7}$$

$$K = (K_{ij}) = \left(\left.\frac{\partial^2 U(x)}{\partial x_i \partial x_j}\right|_{x=x_\mathrm{eq}} \right), \tag{3.8}$$

Table 3.1: The potential for Type B suspension (SR)

potential		term	remarks
U	$U_{\mathrm{wire_s}}$	$\frac{1}{2}k_s(l-l_0)^2$	$k_\mathrm{s} = ES/l_0$
	$U_{\mathrm{wire_t}}$	$\frac{1}{2}k_\mathrm{t}\Delta\theta_\mathrm{t}^2$	$k_\mathrm{t} = JG/l_0$
	U_{GAS}	$\frac{1}{2}M\left(2\pi f_0\right)^2\Delta h^2 + Mg\Delta h$	-
	U_{gravity}	Mgy	-
T	T_{tra}	$\frac{1}{2}M\left(\dot{x}^2+\dot{y}^2+\dot{z}^2\right)$	-
	T_{rot}	$\frac{1}{2}\boldsymbol{\omega}^T I\boldsymbol{\omega}$	-
$\mathscr{F}$	$\mathscr{F}$	$\frac{1}{2}\left(\dot{\boldsymbol{x}}_1-\dot{\boldsymbol{x}}_2\right)^T C\left(\dot{\boldsymbol{x}}_1-\dot{\boldsymbol{x}}_2\right)$	-

Table 3.2: parameters for lagrangian

symbol	meaning
C	suitable damping coefficient matrix
E	Young's modulus
f_0	resonant frequency of GAS
G	shear modulus
Δh	deviation of keystone of the GAS from equilibrium position
I	moment of inertia tensor
J	polar moment of inertia of wire cross section
l	actual distance between two attachment points
l_0	natural length of the wire
M	mass
S	cross section of wire
x	position
y	position
z	position
$\boldsymbol{x}_1$	position and orientation of damper
$\boldsymbol{x}_2$	position and orientation of conducting body
$\Delta\theta$	twist angle
ω	angular velocity

Table 3.3: The design parameter for Type B suspension (SR) from [30]

description		symbol	unit	F0	F1	F2	IRM	IM	RM	TM
body	mass	M	kg	474	90	90	12	16	13	10.7
	momenta of inertia (x)	I_x	kg m^2	60	4	4	0.25	0.15	0.18	0.051
	momenta of inertia (y)	I_y		120	6.4	6.4	0.4	0.19	0.18	0.051
	momenta of inertia (z)	I_z		60	4	4	0.25	0.15	0.23	0.084
wire	number of wires	n	-	-	1	1	3	1	4	4
	material	-	-	-	margin steel		C70 steel	margin steel	tungsten	
	density	ρ	g/cm^3	-	8.0		7.8	8.0	19.3	
	Young's modulus	E	Gpa	-	195		200	195	411	
	Poisson ratio	σ	-	-	0.3		0.3	0.3	0.28	
	loss angle	ϕ	-	-	1×10^{-3}		1×10^{-4}	1×10^{-3}	1×10^{-4}	
	length	L	m	-	1.3	0.56	0.56	0.56	0.56	0.56
	length in sumcon		m							
	diameter	d	mm	-	2.1	1.6	0.3	0.85	0.6	0.2
	diameter in sumcon		mm							
	x position	D_x	mm	-	-	-	-	-	10	5
	z position	D_z	mm	-	-	-	-	-	145	125
	radial distance to y axis	D_r	mm	-	-	-	150	-	-	-
	upper clamp y positon	D_{y_u}	mm	-	-5	5	0	-5	0	0
	lower clamp y position	D_{y_l}	mm	-	-5	5	0	-2	0	0
GAS	resonant frequency	f_{GAS}	mHz	60	250	250	-	-	-	-
	qualiy factor	Q_{GAS}	-	3	6	6	-	-	-	-
	saturation level	B_{GAS}	dB	-60	-60	-60	-	-	-	-
IP	radial distance to y axis	R_{IP}	mm	600	-	-	-	-	-	-
	horizontal mode frequency	f_{IP}	mHz	30	-	-	-	-	-	-
	qualiy factor	Q_{IP}	-	3	-	-	-	-	-	-
	saturation level	B_{IP}	dB	-70	-	-	-	-	-	-

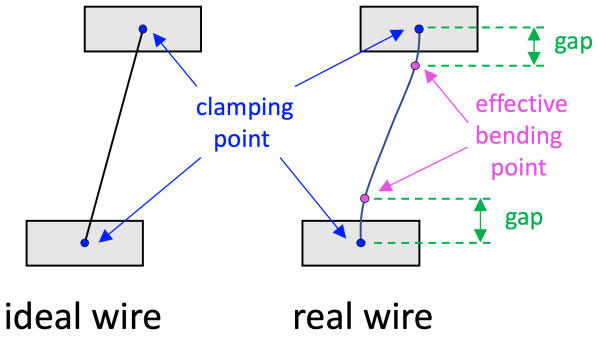

Figure 3.4: The difference of ideal wire and real wire. Real wire has the breakoff because of its rigidity.

where T is kinetic energy, $\mathscr{F}$ is dissipation function and U is the potential energy. M is the inertia matrix, C is the damping matrix and K is the stiffness matrix. As a result, one can get the linearized equation of motion.

From the definiton in subsection 3.1.1, the lagrangian consists of potential energies in table 3.1, table 3.2 and table 3.3. As a result, one can get the transfer functions in all DoFs from the linearized equation. This helps us to know the behavior in frequency space. When one control the system, it is important to get the frequency response of the system. With actuators and sensors, it is possible to actuate the system and get the displacement of the system. The transfer function, G_{ij}, from input i to output j is described as

$$G_{ij} = \left[\left(-\omega^2 M + i\omega C + K\right)^{-1}\right]_{ij} \tag{3.9}$$

and one can get this function from the Fourier transform of the linearized equation,

$$M\ddot{\boldsymbol{x}} + C\dot{\boldsymbol{x}} + K(\boldsymbol{x} - \boldsymbol{x}_{\text{eq}}) = \boldsymbol{F} \tag{3.10}$$

which is eq. (3.5) with excitation term. When one wants a response from ground motion, $\boldsymbol{x}_g$, one can use the transfer function [30],

$$G_{ij}^{(\text{ground})}(\omega) = \left[\left(-\omega^2 M + i\omega C + K\right)^{-1}\left(\omega^2 M_{\text{g}} - i\omega C_{\text{g}} - K_{\text{g}}\right)\right]_{ij}. \tag{3.11}$$

3.1.4 Other Effects

In an ideal model, one can use the ideal wire which is massless and does not have the effective bending point in fig. 3.4. When one clamps a wire, it has a breakoff, Δ [34],

$$\Delta = \sqrt{\frac{EI}{T}} \tag{3.12}$$

where E is the Young's modulus, I is the second moment of area, and T is the tension of the wire. The second moment of area is a geometrical property of an area which reflects the amount representing easiness of deformation of a member with regard to an arbitrary axis. In this case, $I_y = \pi d^4/64$ where y is the axis which penetrates the wire from below.

4 Installation of SR3 and its feature

I have participated in the installation of all Type B suspensions , i.e. BS, SRM, SR2 and SR3 with a team from NAOJ. In this chapter, I mention the feature of SR3 as an example of a Type B suspension.

4.1 Installation of SR3

The summary of the installation process:

Fig. 4.1 shows the installation of the test mass. Before this phase, we put on four permanent magnets for actuating on the mirror and attached four "wire breakers" to hang with wires. In this phase, we set the TM to the nominal position in the assembly frame. To do that, we used a rail on the assembly frame and slided the optic stand.

Fig. 4.2 shows the installation of the intermediate mass. By setting this, one can hang the TM from IM.

Fig. 4.3 shows the installation of the recoil mass. Recoil mass can be divided into the cap part and the body part. After hanging optic, one can cover the optic with the body part of RM. After lid, we also hang the RM.

Fig. 4.4 shows the installation of the standard filter. Since the spring constant of GAS filter depends on the hung mass, we used ballast masses to adjust the horizontal level and the weight. Because GAS filter's resonant frequency also depends on the payload mass, we measured the tolerance range of the payload weight. Fig. **??** shows the result of SR3 BF and the plot draws a parabola around the extreme value.

Fig. 4.5 shows the installation of the Pre-Isolator. First, we calibrated the F0, LVDT and after that we put it on the assembly frame.

Fig. 4.6 shows the hung SR3 to put into the chamber.

Fig. 4.7 shows the rack which includes coil drivers, analog digital converters, digital analog converters and so on. Fig. 4.8 shows the way to accumulate data. All signal go through this rack and then go to the real time machine in the calculator room. The signal is then processed by DAQ computers and sends to the client PCs and data transfer computers. The data transfer computer sends data to the storage system in Kashiwa campus. Since KAGRA sends 20 MB/s, the storage in Kashiwa is 3–5 PB for 5 year data [JGW-G1301945-v2].

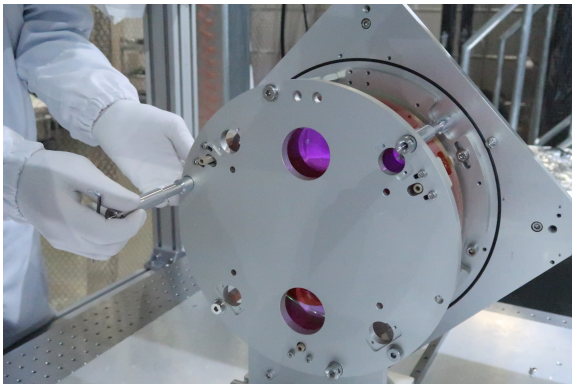

Figure 4.1: Installation of the optic.

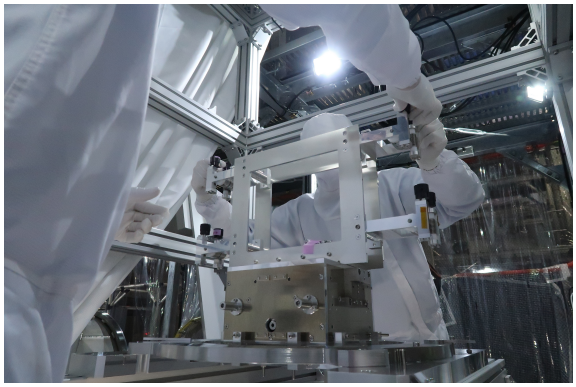

Figure 4.2: Installation of the intermediate mass (IM).

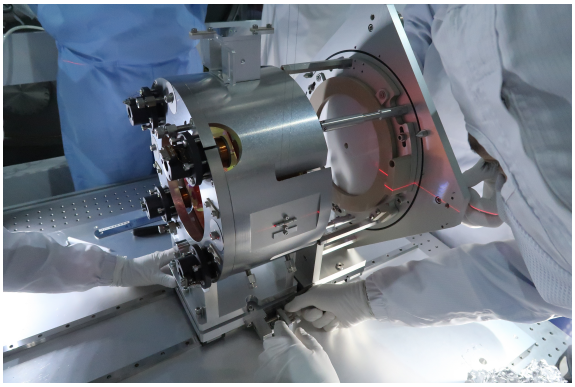

Figure 4.3: Installation of the recoil mass (RM).

Figure 4.4: Installation of the Standard Filter.

Figure 4.5: Installation of the Preisolator.

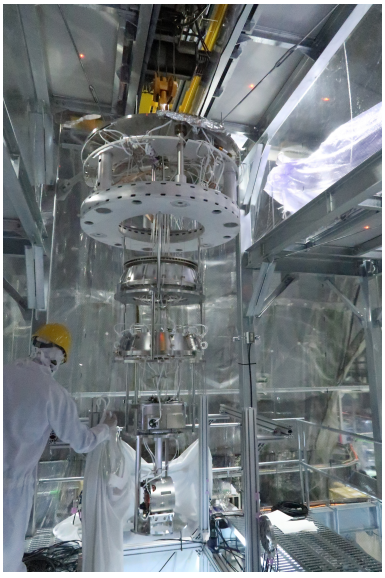

Figure 4.6: Installation of SR3.

Figure 4.7: This is a rack for analog circuit and digital system.

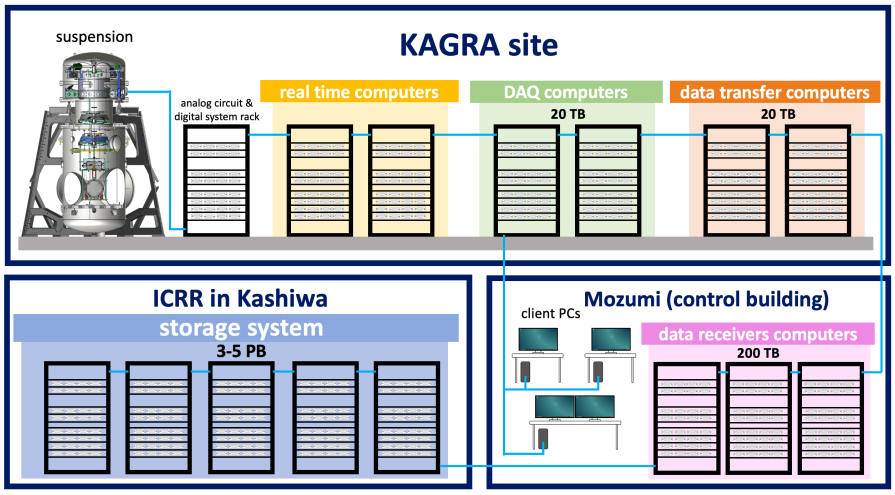

Figure 4.8: Data pass from the interferometer to the storage.

4.2 Features of SR3

4.2.1 LVDT calibration

The LVDT is an electrical transformer used to measure the linear displacement and it's an abbreviation of "Linear Variable Differential Transformer". One important feature of an LVDT is its friction-free operation and thanks to that, it can measure its infinitesimally small changes in the core position [32].

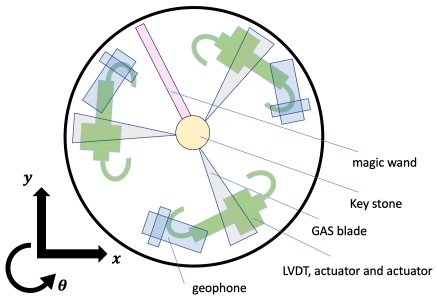

Figure 4.9: Position relation of GAS blades, geophones, LVDTs, actuators and stepper moters

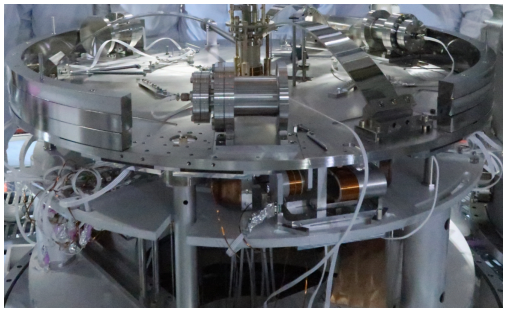

Figure 4.10: Upper part of PreIsolator for SR3

PI

Fig. 4.11 shows the calibration result of SR3 IP LVDTs and table 4.1 shows their calibration factors and linear range. These data are used to convert the value from count to displacement in the control computer. Details are in chapter **??**

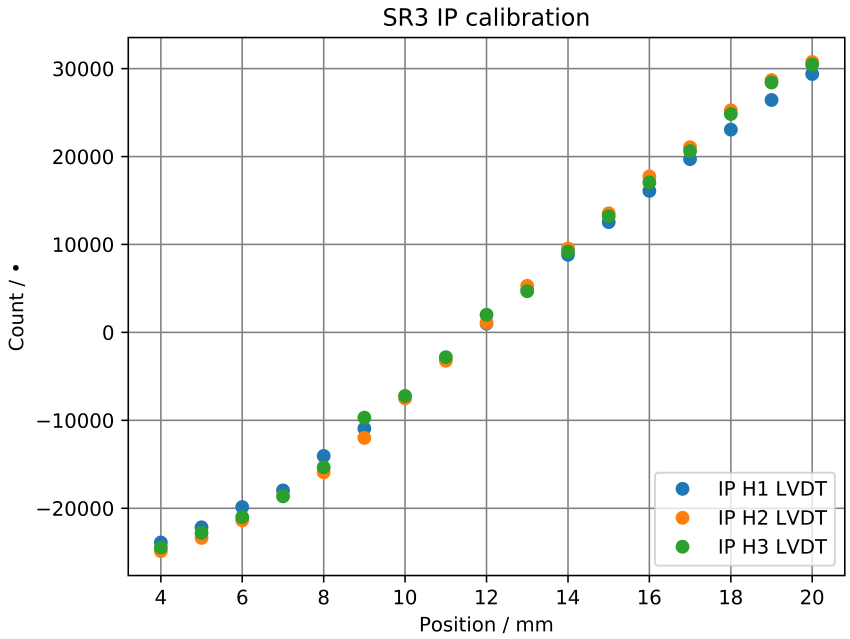

Figure 4.11: LVDTs calibration for SR3 IPs

Table 4.1: Calibration factor and linear range of LVDTs for SR3 IPs

sensor	calibration factor	linear range
LVDT H1	0.262 μm/cnt	7 mm – 17 mm
LVDT H2	0.240 μm/cnt	8 mm – 17 mm
LVDT H3	0.253 μm/cnt	8 mm – 18 mm

GAS

Fig. 4.12 shows the calibration result of SR3 GAS LVDTs and table 4.2 shows their calibration factors and linear range. Every LVDT has enough linear range and the plots are not shifted significantly from the approximate line.

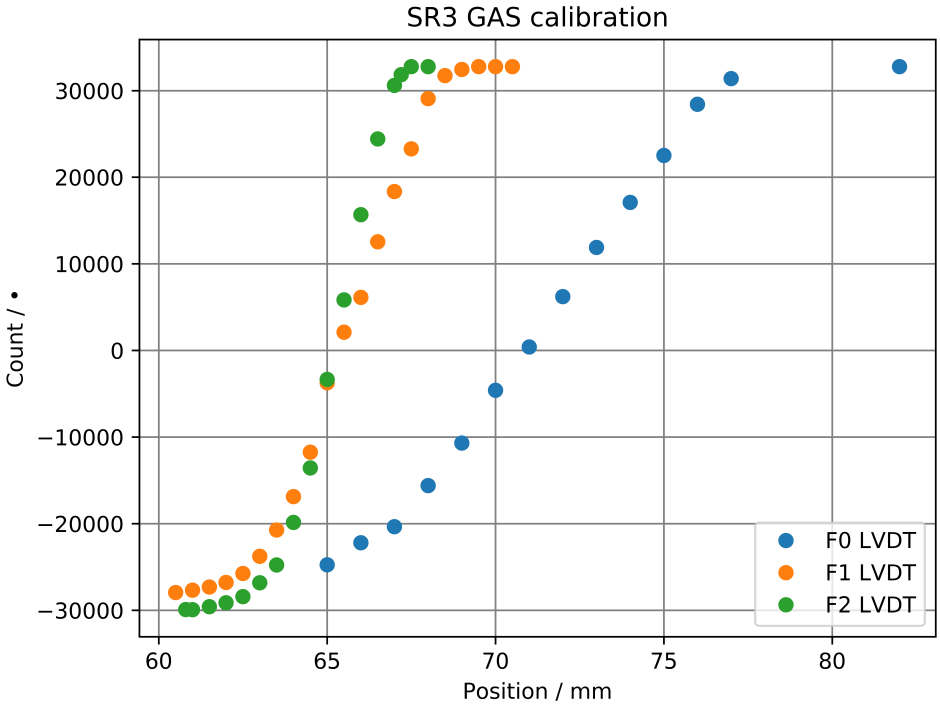

Figure 4.12: LVDTs calibration for SR3 GAS

Table 4.2: Calibration factor and linear range of LVDT for SR3 GAS

sensor	calibration factor	linear range
LVDT F0	0.262 [μm/cnt]	68.0 mm – 76.0 mm
LVDT F1	0.240 [μm/cnt]	63.5 mm – 68.0 mm
LVDT F2	0.253 [μm/cnt]	64.0 mm – 66.5 mm

OSEM

Fig. 4.13 shows the calibration result of SR3 GAS LVDTs and table 4.3 shows their calibration factors and linear range. The liner range of OSEM No. 58 is smaller than those of other OSEMs. However it has 10000 count liner range and the result is sufficient.

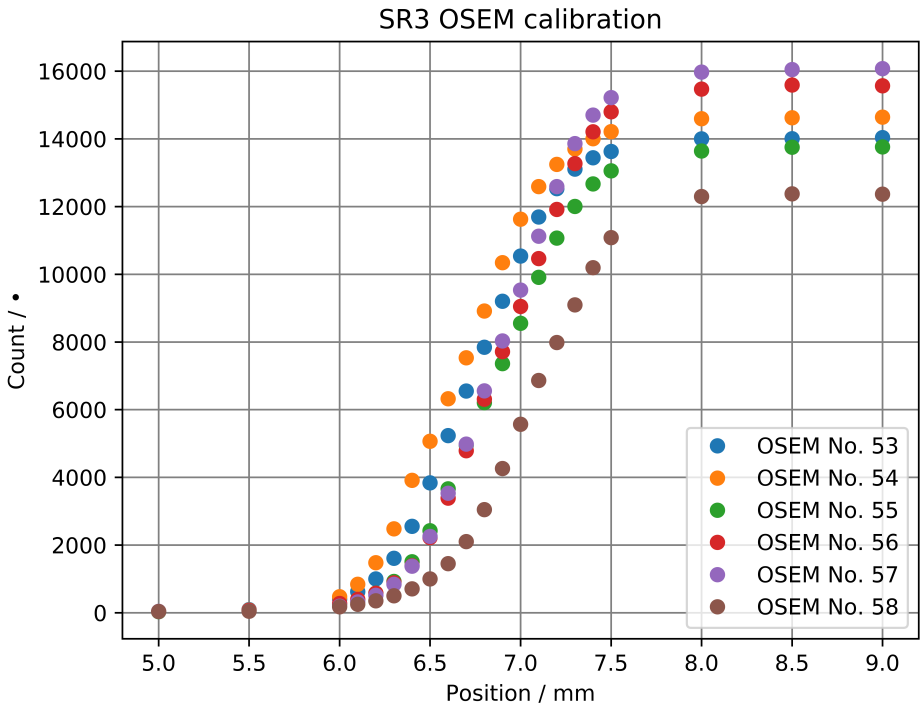

Figure 4.13: OSEM Calibration

Table 4.3: Calibration factor and linear range of LVDT

number	position	calibration factor	linear range
No. 53	IM V1	78.99 nm/cnt	6.3 mm – 7.2 mm
No. 54	IM V2	79.01 nm/cnt	6.2 mm – 7.2 mm
No. 55	IM V3	83.25 nm/cnt	6.4 mm – 7.3 mm
No. 56	IM H1	74.35 nm/cnt	6.4 mm – 7.4 mm
No. 57	IM H2	70.76 nm/cnt	6.4 mm – 7.4 mm
No. 58	IM H3	88.71 nm/cnt	6.6 mm – 7.5 mm

4.2.2 Transfer function

Fig. 4.14 shows the transfer function (TF) of SR3 IP. The top graph shows the magnitude of longitudinal, second one shows the magnitude of transverse and the third one shows the magnitude of yaw. The order of the resonant frequency is 0.1 Hz and it satisfies the requirement. Fig. 4.15 shows the transfer function of SR3 GAS filters. Since important part is around 1 Hz, one can ignore the part which is greater than 10 Hz. This is because the ground vibration is small at high frequency. Fig. 4.16 shows the transfer function of SR3 IM. Blue lines are the transfer functions without damping and orange one with damping (only IM and IPs). In all DOFs, they are damped well. When a suspension is touching, the Q factor becomes small. In this case, all transfer function have large Q factor and it certifies that SR3 is well suspended.

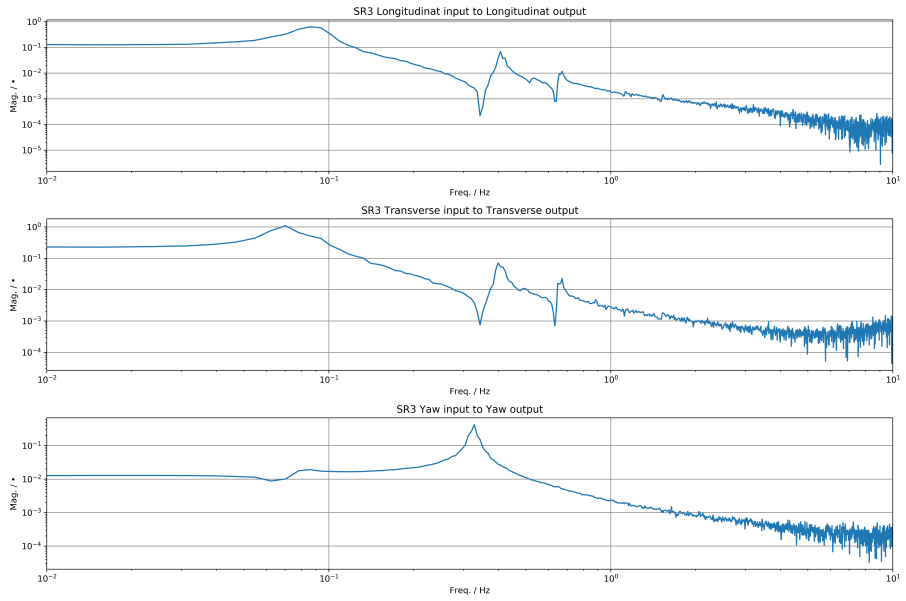

Figure 4.14: Transfer function of SR3 IPs.

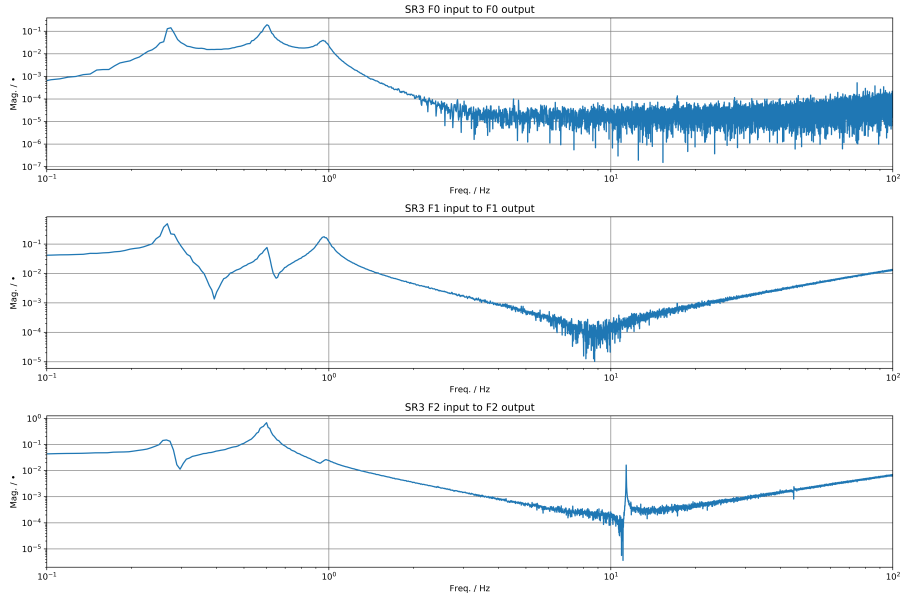

Figure 4.15: Transfer function of SR3 GAS.

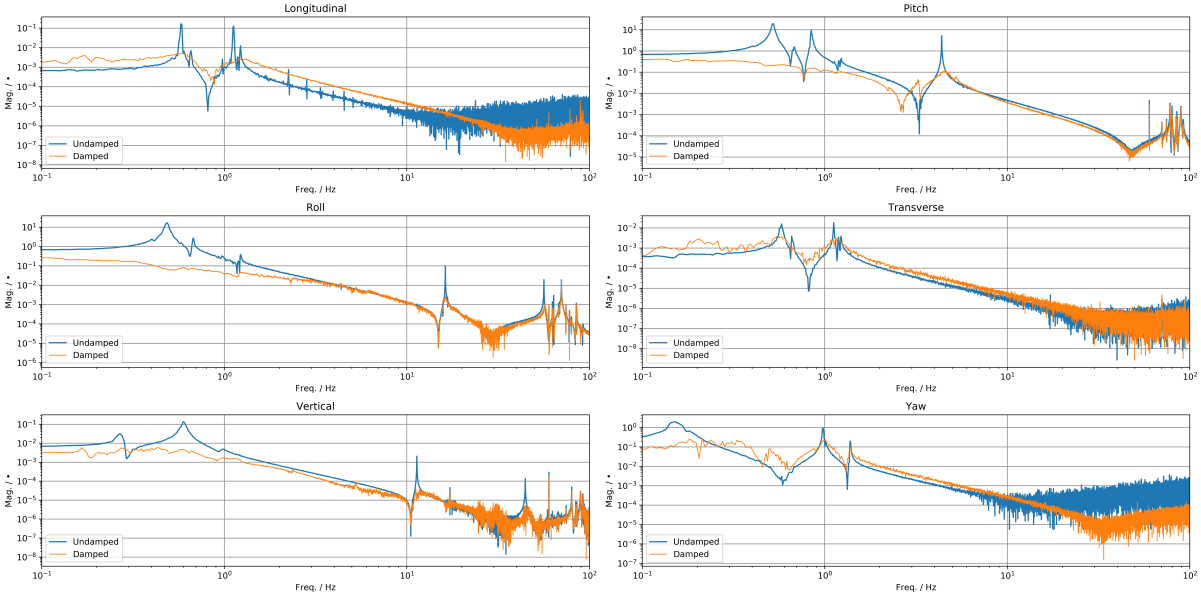

Figure 4.16: Transfer fucntion of SR3 IM.

5 Control System and Simulation

5.1 Control system of Type B suspensions

Fig. 5.1 shows the MEDM screen to control SR3 suspension. Simulink runs in the background and controls the signal path.

5.1.1 Overview of Type B suspension feedback system

Fig. 5.2 shows the sketch of the feedback system of Type B. This is the active control system and it has three main feedback loop, the IP loop (red), the GAS loop (Green) and payload loop (Blue). The IP loop controls the static position of the top stage and damps the pendulum mode. The GAS loop mainly controls the displacement because of the thermal effect. The payload loop controls the structural resonance of the test mirror and aligns the suspension optics.

5.1.2 Details of IM feedback system

Fig. 5.3 shows a cartoon of the feed back system of SR3 IM. The OSEM detects the displacement of IM and then the signal passes through the Analog to Digital Converter (ADC) and becomes the digital signal. In the digital world, the signal is changed its format by the input matrix and then it is injected as an input signal to the control filter. The control filter injects the output signal and it is changed its format by the output matrix. After that, the signal passes through the Digital to Analog Converter (DAC) and becomes the analog signal. Then the analog signal goes to the OSEM coil and the IM gets the feedback signal and is controlled.

5.2 Control theory

5.2.1 Modern Control theory

Classical control is a control system which deals with the performance of the dynamical system. Classical control theory is the one–input one–output system and evaluates the frequency response of the system. On the other hand, Modern control theory uses the first-order ordinary differential equations called state equations. This state equation consists

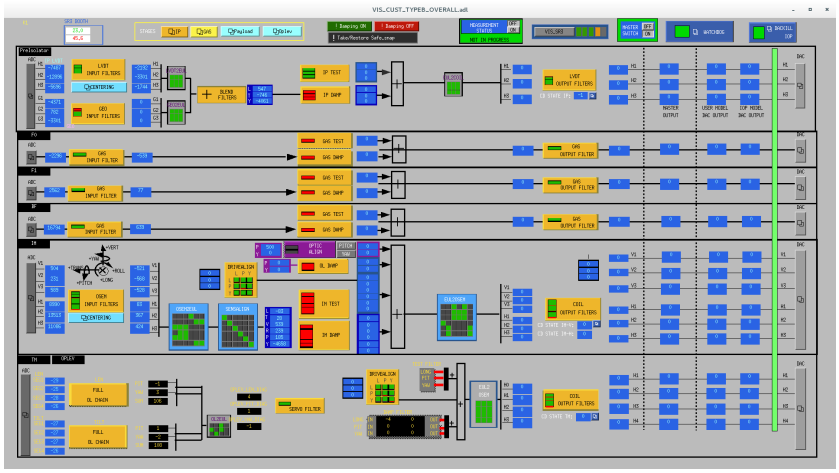

Figure 5.1: MEDM screen to control SR3

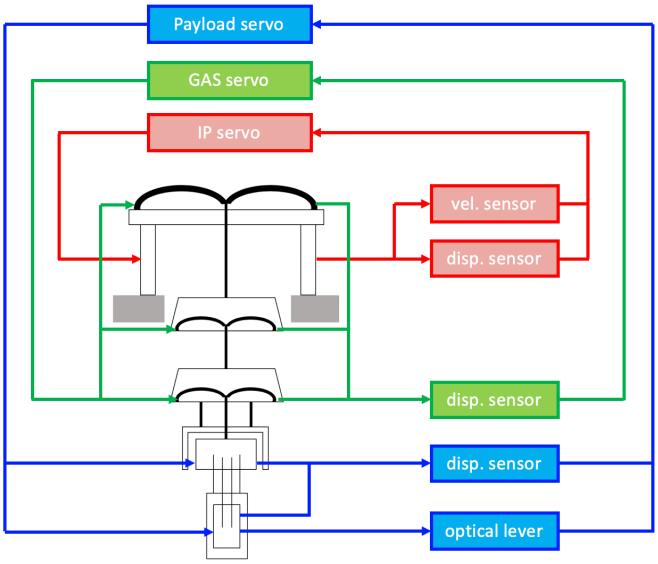

Figure 5.2: Feedback cycle of suspension. [29]

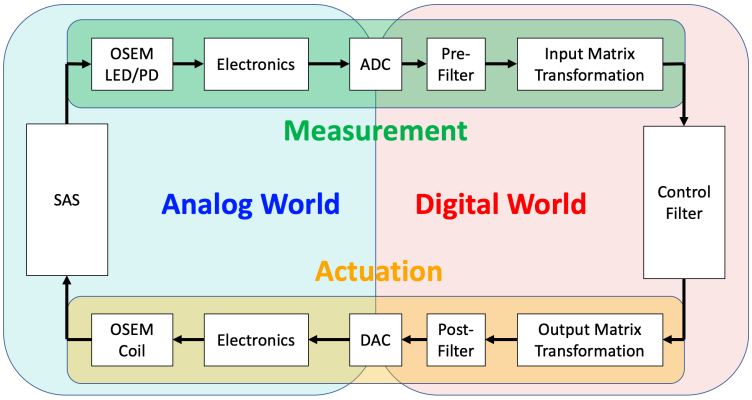

Figure 5.3: Feedback cycle

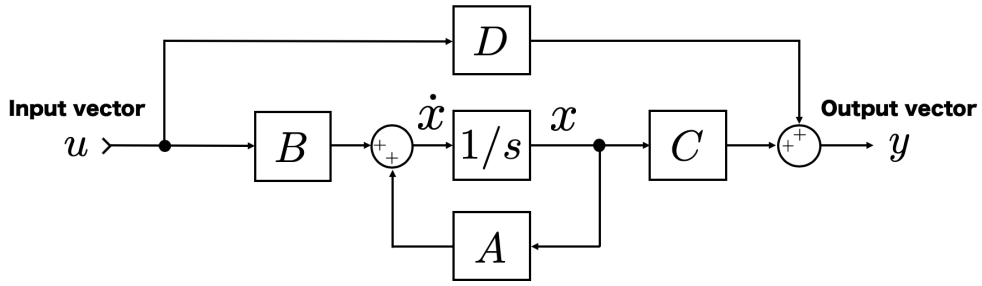

Figure 5.4: Typical control system in a state space representation.

of inputs, outputs and internal states of the system. Fig. 5.4 shows the typical control system in a state space representation. The state equation of this system is described as

$$\begin{cases} \dot{x} = Ax + Bu \\ y = Cx + Du \end{cases}, \tag{5.1}$$

where u is the input signal vector, y is the output signal vector, x is the internal state of the system vector, A is the state matrix, B is the input matrix, C is the output matrix and D is the feedthrough matrix. For example, the equation of motion of the 1 degree of freedom vibration system in fig. 5.5 is described as

$$m\ddot{x} + kx = F, \tag{5.2}$$

and this equation is also described as

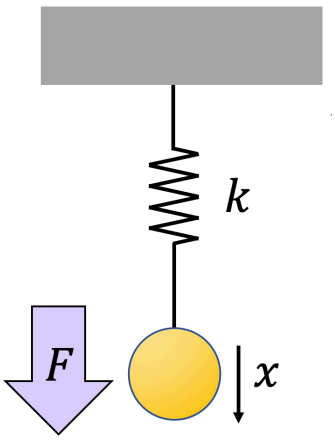

Figure 5.5: single spring vibration system

$$\begin{cases} \dot{\boldsymbol{x}} = \begin{pmatrix} 0 & 1 \\ -km^{-1} & 0 \end{pmatrix} \boldsymbol{x} + \begin{pmatrix} 0 \\ m^{-1} \end{pmatrix} F \\ y = \begin{pmatrix} 1 & 0 \end{pmatrix} \boldsymbol{x} \end{cases} \tag{5.3}$$

$$\tag{5.4}$$

$$\boldsymbol{x} = \begin{pmatrix} \dot{x} \\ x \end{pmatrix}. \tag{5.5}$$

In general, when B is a $n \times 1$ matrix and C is a $1 \times n$ matrix, by Fourier transform of state equation, the transfer function of the system $G(s)$ is described as [1]

$$G(s) = c(sI - A)^{-1}b. \tag{5.6}$$

ABCD matrices also describe the time response of this system,

$$x(t) = e^{At}x_0 + \int_0^t \mathrm{d}\tau e^{A(t-\tau)}Bu(\tau), \tag{5.7}$$

where x_0 is the initial position.

As a conclusion, the ABCD matrices include the information of the system and one can build the model in the state space.

5.3 Model in State Space

In this section, we discuss the SR3 IM Yaw. Yaw is an important degree of freedom. This is because BS separates the injected beam and 1 μrad Yaw motion changes the beam spot at the end test mass 3 mm. Yaw motion control is also important for SRs because SRM has a small mirror and the alignment requirement becomes severe. Furthermore since Yaw motion has less coupling, it is good and easy to check its behavior first.

5.3.1 Transfer function

To measure the transfer function, I used Fast Fourier Transform (FFT) with an application from LIGO, called Diagnostics Test Tools (DTT) which can be seen in fig. 5.6 [33].

The transfer function of SR3 IM Yaw to IM Yaw is shown in fig. 5.7. The peak around 0.1 Hz is from the lack of magnetic damping from the MD to the top filter.

So one can change the magnitude of the peak from the strength of the magnetic damper and change the resonant frequency by changing the stuff value like the width and length of the suspending wire.

5.3.2 Time series

Fig. 5.8 shows the time series of SR3 IM Yaw step response. The injected step function to SR3 IM Yaw was 1000 counts in KAGRA. Because of the system, the injection is not the ideal step function, it has non-neglectable rise time. However, the tilt of the IM changed immediately. Until 20 seconds, it matches but after that, the amplitude of the simulation in Matlab becomes smaller and the frequency drift a little. One possibility of mismatch is the different Q factors between measured data and simulation. The frequency until 20 seconds is 0.1567 Hz and after that, the frequency drifts to 0.1343 Hz. In this phase, it is not easy to evaluate the result quantitatively because now Type B suspensions have just been installed and are going to be more and more characterized and also diagonalized different DoF at the IM and IP stages to meet the requirements.

[1] According to the custom, a $n \times 1$ matrix and a $1 \times n$ matrix are described by small letters.

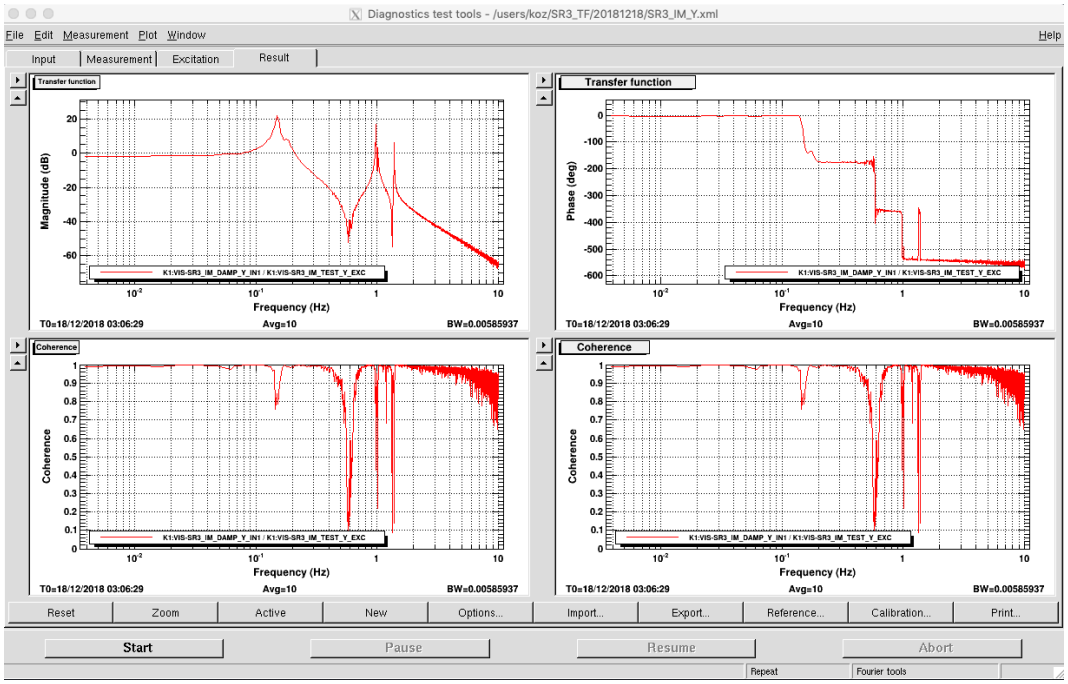

Figure 5.6: DTT is an application which can measure the transfer function and time series. The result is the transfer function of SR3 IM Yaw. The upper left graph shows the magnitude of the transfer function. The upper right graph shows the phase of the transfer function. The lower graph shows the coherence of the transfer function.

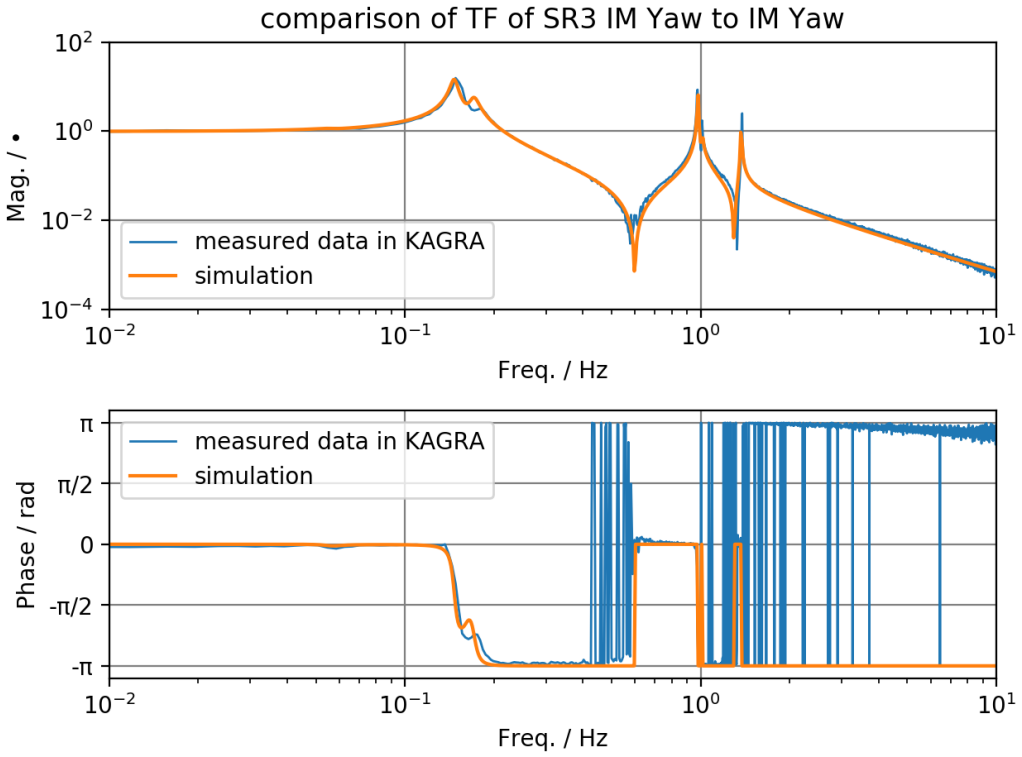

Figure 5.7: The transfer function of SR3 IM Yaw (input) to IM Yaw (output).

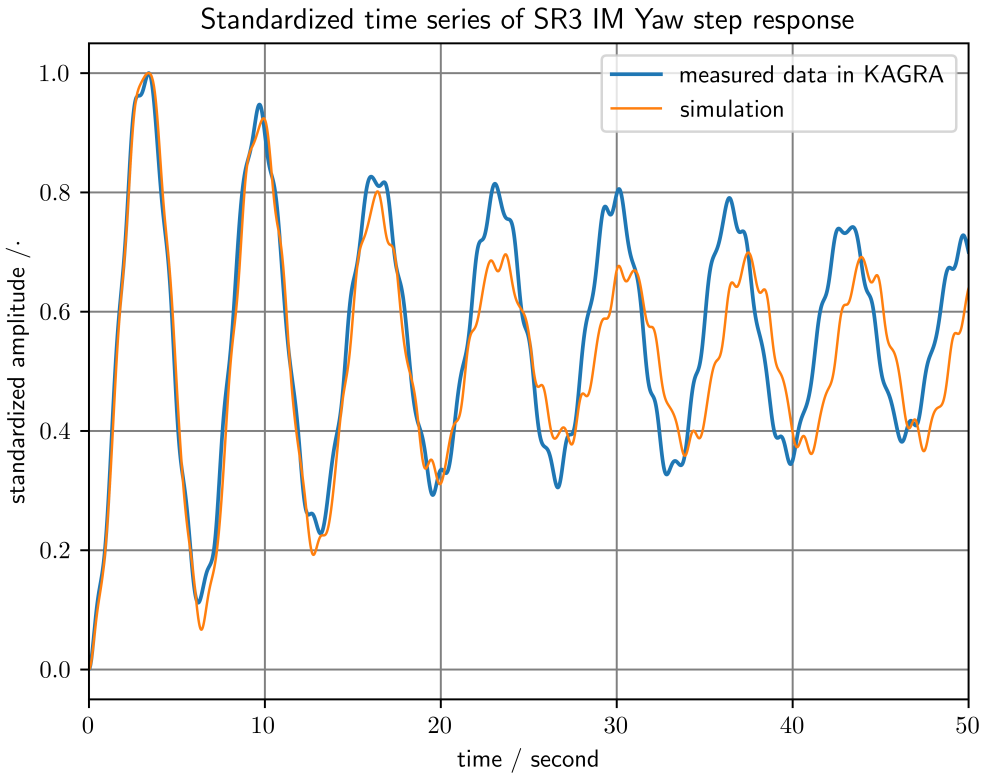

Figure 5.8: The comparison of time series of SR3 IM Yaw (input signal is step function).

6 Summary

I made significant contributions to the installation of all the type B suspensions which are critical building blocks of KAGRA. Since not only the type B but also the rest of the suspensions are installed in KAGRA today, KAGRA is now ready for the subsequent commissioning tests which then make it operational. Observation 3 (O3) is an upcoming joint observing run by four detectors, LIGO (Hanford and Livingston), VIRGO and KAGRA. In the nominal plan, O3 starts from this April with three detectors, namely LIGO (Hanford and Livingstone) and VIRGO. Subsequently, KAGRA is going to join O3 from the second half of this year.

While no one is allowed to actively test the suspensions in KAGRA during O3, we need to start considering the upgrade for Observation 4 (O4) with the existing instruments. Therefore, it is useful to build a model of suspensions in state space so that one can simulate and/or update the model of suspension even during O3.

I built a model for one of the mechanical degrees of freedom, namely yaw in the IM stage, of SR3 in state space. The model was able to successfully reproduce actual behavior of the suspension in time domain when a step excitation force was applied to the IM yaw. However, the simulated data also showed discrepancy from the actual behavior after 20 seconds elapsed. This seems to be due to the fact that they are not yet fully characterized nor diagonalized completely. This suggests that we need to work more on the characterization of the system in order to fully exploit the state space approach.

Future works include the expansion of the model to include the rest of degrees of freedom, incorporation of cross-couplings between various degrees of freedom, precise system identification and so forth. These will make the model applicable to various experiments and thus useful.

My study presented in this thesis is essential not only for accelerating the installation activities in KAGRA, but also for advancing the suspension design which is a key for the gravitational wave detectors.

Acknowledgement

First of all, I thank Prof. Takaaki Kajita for giving me the environment to work in KAGRA. It was a sensational place for me and I enjoyed the discussion with many researchers. In KAGRA I learned how to find and solve problems. I am grateful to all the people involved in KAGRA.

I thank the people who worked with me in VIS Type B team – Mark Barton, Fabian Peña, Enzo Tapia and Naoatsu Hirata. Additionally, special helps for Type B team – Yoichi Aso, Ayaka Shoda, Naoko Oishi, Yoshinori Fuji and Toshiya Yoshioka. Mark Barton is a researcher from NAOJ and a team leader of the type B team. He used to work in LIGO in the USA. He is a vibration isolation suspension expert and he is good at building a mathematical model of suspension. I sometimes referenced his documents. Fabian is a researcher from ICRR[1]. Cabling of suspensions is one of the most annoying and difficult work. He and I sometimes discuss how to cable. Enzo is an engineer from NAOJ and well acquaints with physics. We discussed many topics and I think I spent the longest of the time with him in the team. Hirata san is an engineer from NAOJ and he is good at parts for building a suspension. When I heard about the parts he explained me carefully and that helped me. Yoichi Aso introduced many things to me. This thesis topic is one of that. Kiwamu Izumi is an interferometer expert and he also gave me many interesting physics ideas. I am grateful to Yoshinori Fuji who supported me when I took data and analyzed them. He and I sometimes discuss in late time and he gave me a lot of advice and knowledge.

Finally I would like to express my gratitude to my family. I have been able to write this paper now because of their economic and kind support. Thanks to my family, I have been able to stay in Toyama and concentrate on the research.

[1]He belonged to NAOJ until March 2018.

Bibliography

[1] A. Einstein, "Grundgedanken der allgemeinen Relativitätstheorie und Anwendung dieser Theorie in der Astronomie", itzungsber. Preuss. Akad. Wiss. Berlin, 315 (1915) i, 1

[2] A. Einstein, "Zur allgemeinen Relativitätstheorie", Sitzungsber. Preuss. Akad. Wiss. Berlin (Math. Phys.), 778, 799 (1915) i, 1

[3] B. P. Abbott et al., "Observation of Gravitational Waves from a Binary Black Hole Merger", Phys. Rev. Lett. **116**, 061102 (2016). i, 3, 4

[4] A. Einstein, "Näherungsweise Integration der Feldgleichungen der Gravitation" Sitzungsber. K. Preuss. Akad. Wiss. 1, 688 (1916). 1

[5] M. Maggiore, "Gravitational Waves Vol. 1: Theory and Experiments", Oxford University Press. 2

[6] B. P. Abbott et al., https://dcc.ligo.org/LIGO-P1800307/public 3

[7] K. Belczyński, V. Kalogera, and T. Bulik, "K. Belczyński, V. Kalogera, and T. Bulik, A Comprehensive Study of Binary Compact Objects as Gravitational Wave Sources: Evolutionary Channels, Rates, and Physical Properties", The Astrophysical Journal, **572**(1):407-431, (2002). 3

[8] LIGO Scientific Collaboration et al., "Predictions for the Rates of Compact Binary Coalescences Observable by Ground-based Gravitational-wave Detectors" Classical and Quantum Gravity, **27**(17):173001, (2010). 3

[9] B. S. Sathyaprakash and B. F. Schutz, "Physics, astrophysics and cosmology with gravitational waves", Living Reviews in Relativity, **12**, (2009). 3

[10] K. N. Yakunin et al. "Gravitational waves from core collapse supernovae" Class. Quantum Gravity **27**, 194005 (2010) 3

[11] C. Grupen. "宇宙素粒子物理学 (Astroparticle Physics)", 丸善出版 (MARUZEN PUBLISHING) (2012) 3

[12] R. A. Hulse and J. H. Taylor, "Discovery of a pulsar in a binary system", Astrophys. J. **195**, L51 (1975). 4

[13] J. H. Taylor, J. M. Weisberg, "Further experimental tests of relativistic gravity using the binary pulsar PSR1913+16", Astrophys. J. **253**, 908 (1982)) 4

[14] J. Weber, “Evidence for Discovery of Gravitational Radiation”, Phys. Rev. Lett. **22**, 1320 (1969). 4

[15] T. Nakamura, N. Mio, and M. Ohashi, “重力波をとらえる”, Kyoto University Press, (1998). (in Japanese). 5

[16] K. Izumi, PhD. thesis, Univ. of Tokyo, (2012) https://dcc.ligo.org/LIGO-P1300001/public 5, 6

[17] K. Yamamoto et al., “Measurement of seismic motion at Large-scale Cryogenic Gravitational wave Telescope project site”, https://gwdoc.icrr.u-tokyo.ac.jp/cgi-bin/DocDB/ShowDocument?docid=218 7, 9

[18] K. Nagano, “A study on the reduction of quantum noise for the gravitational wave detector KAGRA” http://granite.phys.s.u-tokyo.ac.jp/knagano/html/koji.html 7

[19] K. Yamamoto, master thesis, Univ. of Tokyo (1997) “TAMA300 の Suspension System 及び鏡の熱雑音の推定”, http://granite.phys.s.u-tokyo.ac.jp/ja/?MasterTheses 8

[20] M. Ando, “Fabry-Pérot 型レーザー干渉計重力波検出器の制御”, http://granite.phys.s.u-tokyo.ac.jp/ja/?MasterTheses 8

[21] Y. Saito and R. Takahashi, “Production Process of the Interferometer Beam Tubes in LCGT Project”, J. Vac. Soc. Jpn. Volume 54 Issue 12 Pages 621-626 (2011) 8

[22] Rainer Weiss, “Electromagnetically Coupled Broadband Gravitational Antenna” LIGO-P720002-01-R, 9

[23] G. E. Moss, L. R. Miller, and R. L. Forward, “Photon-Noise-Limited Laser Transducer for Gravitational Antenna”, Applied Optics Vol. 10, Issue 11, pp. 2495-2498 (1971). 9

[24] Xing Zhang, Jiming Yu, Tan Liu, Wen Zhao, and Anzhong Wang, “Testing Brans-Dicke gravity using the Einstein telescope”, Phys. Rev. D **95**, 124008 9

[25] B. P. Abbott et al., “Exploring the Sensitivity of Next Generation Gravitational Wave Detectors”, arXiv:1607.08697v3 9

[26] K. Kuroda and LCGT collaboration, “LARGE-SCALE GRAVITATIONAL WAVE TELESCOPE (LCGT)”, Int. J. Mod. Phys. D, **20** (10), 1755-1770, (2011). 9

[27] B. P. Abbot et al., “Prospects for observing and localizing gravitational-wave transients with Advanced LIGO, Advanced Virgo and KAGRA” Living Rev Relativ (2018) 21: 3. 10

[28] Y. Enomoto, “MIF orientation 2018 ” https://gwdoc.icrr.u-tokyo.ac.jp/cgi-bin/private/DocDB/ShowDocument?docid=837215

[29] T. Sekiguchi, PhD. thesis “A Study of Low Frequency Vibration Isolation System for Large Scale Gravitational Wave Detectors” 16, 18, 19, 21, 29, 42

[30] T. Sekiguchi, Master thesis "Modeling and Simulation of Vibration Isolation System for Large-scale Cryogenic Gravitational-wave Telescope (LCGT)" 28, 31, 32

[31] M. Barton "Cavity Optics Suspension Subsystem Design Requirements Document" LIGO Internal Document, T010007-05, (2008) 28

[32] "LVDT Tutorial" https://www.te.com/usa-en/industries/sensor-solutions/insights/lvdt-tutorial.html 35

[33] G. Hammond, "Update On The Flexure Design" LIGO Internal Document, T010171-00-D, (2001). 32

[34] "Electronic Setup and Testing of Advanced LIGO Suspensions" LIGO Document E1000078-v1 44